Nucleic Acids Research, 2026, **54**, gkag641
https://doi.org/10.1093/nar/gkag641
Gene regulation, Chromatin and Epigenetics

ATF4 and CHOP coordinate endoplasmic reticulum stress-responsive gene programs through enhancer activation and chromatin looping

Jung-Sik Joo[1,2], Mikyoung Kim[1], Sugyung Kim[1,2], Hyejin Kim[1,2], Hyoung-Pyo Kim[1,2,3,*]

[1]Department of Tropical Medicine, Institute of Tropical Medicine, Yonsei University College of Medicine, 50-1 Yonsei-ro, Seodaemun-gu, Seoul 03722, Republic of Korea
[2]Brain Korea 21 PLUS Project for Medical Science, Yonsei University College of Medicine, 50-1 Yonsei-ro, Seodaemun-gu, Seoul 03722, Republic of Korea
[3]Yonsei Genome Center, Yonsei University College of Medicine, 50-1 Yonsei-ro, Seodaemun-gu, Seoul 03722, Republic of Korea
*To whom correspondence should be addressed. Tel: +82 2 2 2281842; Fax: +82 2 363 8676; Email: kimhp@yuhs.ac

Abstract

Endoplasmic reticulum (ER) stress triggers transcriptional programs that promote either adaptation or apoptosis, yet the epigenetic mechanisms underlying this response remain incompletely understood. Here, integrated multi-omics analyses of unfolded protein response transcription factor knockout cells identify ATF4 as a dominant regulator of ER stress-responsive enhancer activation and chromatin looping. Loss of ATF4 markedly impairs stress-induced H3K27ac accumulation and enhancer–promoter interactions at ATF4-associated regulatory elements, establishing ATF4 as a central organizer of the stress-responsive regulatory landscape. We further identify CHOP as a key functional partner of ATF4 during ER stress. Integrative analyses of ATF4 occupancy and H3K27ac landscapes in CHOP-knockout cells reveal that CHOP selectively modulates ATF4-dependent enhancer activity and controls distinct subsets of stress-responsive genes. This cooperation preferentially promotes apoptosis-associated transcriptional programs while having limited effects on core adaptive responses. Together, our findings define a hierarchical regulatory framework in which ATF4 establishes enhancer activation and chromatin looping networks, whereas CHOP selectively diversifies their output to specify ER stress-responsive gene programs.

Graphical abstract

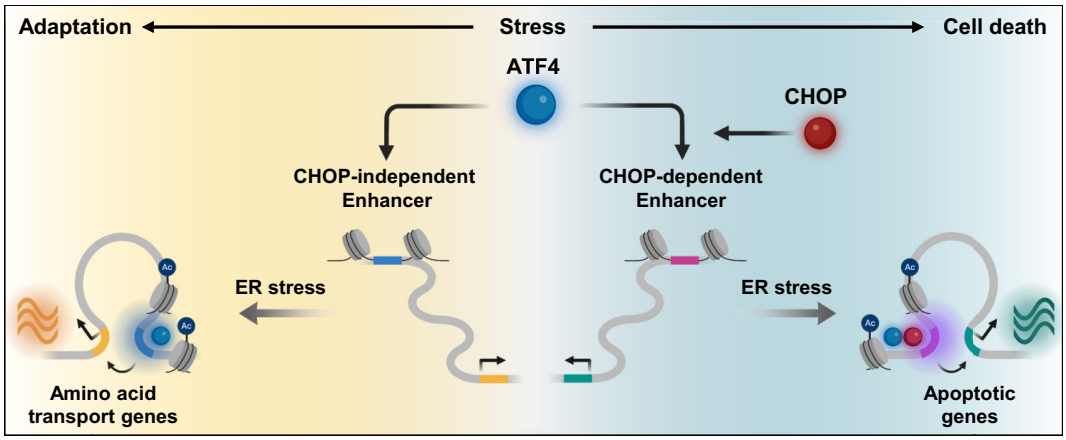

Introduction

Cells respond to endoplasmic reticulum (ER) stress by activating the unfolded protein response (UPR), a signaling network that restores proteostasis and, depending on stress intensity and duration, promotes either adaptive or apoptotic responses [1, 2]. In metazoans, the UPR is mediated by three major ER-resident stress sensors—protein kinase R-like ER kinase (PERK), inositol-requiring enzyme 1 (IRE1), and activating transcription factor 6 (ATF6)—which together coordinate programs that reduce protein-folding burden, expand ER capacity, and restore homeostasis [3]. Among these pathways, the PERK–eIF2α axis is a central regulator

Received: April 9, 2026. **Revised:** June 2, 2026. **Accepted:** June 5, 2026

of stress-induced gene expression through selective translational induction of ATF4 and its downstream effector CHOP [4, 5].

Each branch of the UPR contributes distinct but partially overlapping transcriptional programs [6, 7]. ATF4 regulates genes involved in amino acid transport, redox control, proteostasis, and metabolism, whereas CHOP has frequently been linked to unresolved stress and apoptosis. In parallel, the IRE1–XBP1 and ATF6 branches activate transcriptional programs associated with ER folding, secretion, and quality control. Together, these pathways establish a multi-layered signaling system capable of generating diverse transcriptional responses under ER stress. However, how such signaling diversity is encoded within the regulatory genome remains incompletely understood.

Previous efforts to define UPR target genes have largely relied on promoter-centric approaches, including transcription factor (TF) binding at proximal promoters and transcriptional changes following TF depletion or overexpression [8–11]. While informative, these strategies do not readily distinguish direct regulatory interactions from secondary transcriptional effects and do not capture the contribution of distal regulatory elements [12, 13]. These limitations are particularly relevant for stress biology, where rapid and selective transcriptional reprogramming may depend not only on promoter occupancy but also on inducible enhancer activity and long-range regulatory interactions.

Emerging evidence indicates that ER stress can induce widespread enhancer activation and dynamic changes in chromatin looping [14–17]. However, the extent to which these chromatin-level changes actively instruct UPR-responsive gene expression, rather than simply accompany it, remains unclear. In particular, how stress-activated TFs coordinate enhancer activity and chromatin interactions to shape gene expression programs has not been systematically investigated.

Many UPR-associated TFs belong to the basic leucine zipper (bZIP) family, whose members regulate gene expression through homo- and heterodimerization [18–21]. Partner choice can markedly alter DNA-binding specificity and diversify transcriptional output, including through heterodimer-specific binding preferences. ATF4, in particular, forms context-dependent heterodimers with multiple bZIP partners, including CHOP and members of the C/EBP family, suggesting that cooperative interactions may diversify enhancer regulation during ER stress [22–27]. Yet, how such interactions contribute to enhancer activity and chromatin looping to generate distinct transcriptional outputs remains unclear.

Here, we combined multilayered epigenomic profiling with genetic perturbation to investigate how ER stress-responsive TFs regulate enhancers and chromatin looping. By integrating RNA-seq, ATAC-seq, H3K27ac ChIP-seq, TF ChIP-seq, Hi-C, and H3K27ac HiChIP with loss-of-function analyses, we sought to define the regulatory architecture underlying ER stress-induced transcriptional reprogramming. Our analyses revealed widespread enhancer activation and dynamic changes in chromatin looping under ER stress and highlighted key contributions of UPR-associated TFs to enhancer-dependent transcriptional regulation, providing a framework for understanding how ER stress-responsive gene (ESRG) programs are organized across the regulatory genome.

Materials and methods

Cell culture and ER stress induction

HCT116 cells (ATCC, CCL-247) were obtained from the American Type Culture Collection and maintained in RPMI-1640 medium (Welgene) supplemented with 10% fetal bovine serum (Hyclone, SH30071.03) and 1% penicillin–streptomycin (Hyclone, SV30010) at 37°C with 5% CO_2. Cells were routinely tested for mycoplasma contamination by polymerase chain reaction (PCR) (iNtRON, 25235). For ER stress induction, cells were treated with tunicamycin (Tm; Sigma–Aldrich, T7765) at a final concentration of 0.5 μg ml^{-1} for 6 h. Vehicle control cells were treated with 0.1% dimethyl sulfoxide (DMSO) for the same duration. The concentration and duration were selected based on preliminary experiments confirming robust UPR activation without affecting cell viability.

Cell viability assay

Cell viability was measured using the CellTiter-Glo® Luminescent Cell Viability Assay (Promega, G7571) according to the manufacturer's instructions. HCT116 cells (5×10^3) were seeded in 96-well plates. After 24 h, cells were treated with Tm (0.5 μg ml^{-1}). At the selected time points (0, 2, 4, 8, 16, and 24 h), 100 μl of CellTiter-Glo reagent was added to each well. Plates were incubated at room temperature for 10 min, and luminescence was measured using a microplate luminometer (Berthold Centro XS3 LB 960) and MikroWin2000 software.

Quantitative PCR

Total RNA was isolated from HCT116 cells using Hybrid-R RNA Purification Kit (GeneAll Biotechnology, 305-101) according to the manufacturer's instructions. RNA was reverse transcribed using PrimeScript™ RT Master Mix (Takara Bio, RR036A). The resulting complementary DNAs (cDNAs) were subjected to quantitative real-time-PCR using QuantStudio3 (Applied Biosystems); the synthesis of double-stranded DNA was monitored during various PCR cycles using QuantiNova SYBR Green PCR Kit (Qiagen, 208052). For each sample, duplicate test reactions were analyzed to determine the expression of the gene of interest, and the results were normalized to *GAPDH* mRNA levels. The primer sequences are listed in Supplementary Table S1.

Western blot analysis

HCT116 cells were lysed in T-PER™ Tissue Protein Extraction Reagent (Thermo Fisher Scientific, 78510) with protease and phosphate inhibitor cocktail (Thermo Fisher Scientific, 78440). Proteins were separated using sodium dodecyl sulfate–polyacrylamide gel electrophoresis and transferred onto polyvinylidene fluoride membrane. After blocking with 5% skim milk, the membrane was incubated with primary antibodies at 1:1000 dilution: ATF4 (Cell Signaling Technology, 11815), CHOP (Cell Signaling Technology, 2895), NFIL3 (Cell Signaling Technology, 14312), C/EBPβ (Santa Cruz Biotechnology, sc-7962), α-tubulin (Santa Cruz Biotechnology, sc32293), ATF6 (Abcam, ab227830), and XBP1 (BioLegend, 647502), followed by incubation with horseradish peroxidase-conjugated secondary antibody at 1:2000 dilution: HRP-linked anti-Rabbit IgG (7074) and HRP-linked anti-Mouse IgG (7076) (Cell Signaling Technology). The target proteins were visualized using Pierce Western Blotting

Substrate (Thermo Fisher Scientific, 32132) and Image Quant LAS 4000 (GE Healthcare).

Generation of knockout cell line

To generate ATF4, ATF6, and XBP1 knockout cell lines, homology-directed repair (HDR)-mediated genome editing was performed. HDR donor templates containing ~600 bp homology arms were constructed and subcloned into knockout donor plasmids (OriGene, KN201959LP, and KN201959RB). Guide RNAs (gRNAs) targeting genomic sequences between the homology arms were cloned into the pX330 vector (Addgene, #42230) using BbsI digestion. For generation of CHOP, C/EBPβ, and NFIL3 knockout cell lines, a dual-gRNA deletion strategy was used to excise coding regions spanning 530–1700 bp. gRNAs were cloned into the pX459 vector (Addgene, #62 988) and combined into a single vector expressing two gRNAs. Wild-type (WT) HCT116 cells were co-transfected with donor plasmids and pX330 constructs, or with dual-gRNA pX459 constructs, as appropriate. Following transfection, cells were selected with puromycin (1 μg ml^{-1}) and blasticidin (8 μg ml^{-1}) for 10–12 days. Individual colonies were isolated and screened by genomic PCR, followed by quantitative PCR (qPCR) and western blot analysis to confirm loss of gene expression. gRNA and genotyping primer sequences are provided in Supplementary Tables S2 and S3.

RNA-seq library preparation

Total RNA was extracted from WT and TF knockout HCT116 cells using RiboEx (GeneAll Biotechnology) according to the manufacturer's instructions. RNA-seq libraries were prepared using NEBNext Ultra RNA Library Prep Kit for Illumina (New England Biolabs, E7760) as previously described [28], with minor modifications. Briefly, poly(A)+ RNA was isolated from 1 μg of total RNA and fragmented, followed by first- and second-strand cDNA synthesis. After adaptor ligation and PCR amplification, libraries were purified using AMPure XP beads and sequenced on an Illumina NovaSeq 6000 platform to generate 100-bp paired-end reads. Three biological replicates were generated for each condition.

ATAC-seq library preparation

ATAC-seq libraries were prepared using the OMNI-ATAC protocol as previously described [28] and sequenced on an Illumina NovaSeq 6000 platform to generate 100-bp paired-end reads. Two biological replicates were generated for each condition.

ChIP-seq library preparation

ChIP-seq experiments were performed as previously described [28], with minor modifications. Cells were cross-linked with 1% formaldehyde and chromatin was sheared by sonication. Immunoprecipitation was performed using antibodies against H3K27ac (Abcam, ab4729), ATF4 (Cell Signaling Technology, 11815), ATF6 (Abcam, ab227830), XBP1 (BioLegend, 647502), CHOP (Cell Signaling Technology, 2895), C/EBPβ (Santa Cruz Biotechnology, sc-7962), and NFIL3 (MBL, PM097). Following immunoprecipitation, tagmentation was performed directly on bead-bound chromatin using Nextera DNA Library Prep Kit (Illumina). Libraries were PCR-amplified, size-selected, and sequenced on an Illumina NovaSeq 6000 platform to generate 100-bp paired-end reads. Two biological replicates were generated for each condition.

In situ Hi-C library preparation

In situ Hi-C was performed as previously described [28]. Briefly, cross-linked chromatin was digested with DpnII, end-filled with biotinylated nucleotides, and ligated under dilute conditions. Following sonication and reverse cross-linking, DNA was purified and subjected to biotin pull-down. Sequencing libraries were generated by tagmentation on bead-bound DNA, followed by PCR amplification and size selection. Libraries were sequenced on an Illumina NovaSeq 6000 platform to generate 100-bp paired-end reads. Two biological replicates were generated for each condition.

HiChIP library preparation

HiChIP was performed as previously described [28], with modifications to capture stress-responsive enhancer interactions. Cells were cross-linked with 1% formaldehyde and chromatin was digested with DpnII, followed by biotin fill-in and proximity ligation. Following sonication, immunoprecipitation was performed using antibodies against H3K27ac (Abcam, ab4729) and ATF4 (Cell Signaling Technology, 11815). Chromatin–antibody complexes were captured, reverse cross-linked, and purified. Purified DNA was subjected to streptavidin bead enrichment, followed by tagmentation and PCR amplification. Libraries were size-selected using AMPure XP beads and sequenced on an Illumina NovaSeq 6000 platform to generate 100-bp paired-end reads. Two biological replicates were generated for each condition.

RNA-seq data processing

Paired-end RNA-seq reads were trimmed using TrimGalore (v0.6.4) and aligned to the human reference genome (hg19) using STAR [29] (v2.6.0c) with the parameters –chimSegmentMin 20 –twopassMode Basic –quantMode TranscriptomeSAM. Gene-level expression was quantified using RSEM (v1.3.1) [30] and normalized to transcripts per million (TPM). Strand-specific reads were extracted using SAMtools (v1.3.1) [31], and genome-wide coverage tracks were generated using deepTools (v3.4.3) [32]. Genes with a mean TPM > 1 were considered to be expressed. Differential gene expression analysis was performed using DESeq2 (v1.44.0) [33] with thresholds of $|\log_2(\text{fold change})| > 0.5$ and false discovery rate (FDR) < 0.05. Significantly upregulated protein-coding genes were defined as ESRGs. Gene ontology (GO) enrichment analysis was performed using clusterProfiler (v4.12.6) [34] with an FDR cutoff of 0.05 and the top enriched terms were visualized.

ATAC-seq data processing

ATAC-seq data were processed as previously described [28]. Paired-end reads were trimmed using TrimGalore and aligned to the hg19 reference genome using Bowtie2 (v2.3.5.1) [35] with parameters –end-to-end –very-sensitive –maxins 2000. Low-quality reads (MAPQ < 30), duplicate reads, and mitochondrial reads were removed using SAMtools and Picard. To correct for Tn5 insertion bias and enrich nucleosome-free regions, reads were processed using alignmentSieve from deepTools with parameters –maxFragmentLength 140 –ATACshift. Peaks were called using MACS2 (v2.2.7.1) [36]

without input control, followed by differential accessibility analysis using DESeq2 with thresholds of $|\log_2(\text{fold change})| > 0.5$ and FDR < 0.05. Normalized bigWig files were generated using deepTools, and biological replicates were merged for visualization and comparative analysis.

ChIP-seq data processing

ChIP-seq data were processed as previously described [28], with minor modifications. Paired-end reads were trimmed using TrimGalore and aligned to the hg19 genome using BWA [37] (v0.7.17). Low-quality reads (MAPQ < 30), duplicate reads, and mitochondrial reads were removed using SAMtools and Picard. Normalized coverage tracks (bigWig) were generated using deepTools. Peaks were called using MACS2 with parameters -f BAMPE –nomodel -g hg19 -q 0.001, and differential peak analysis was performed using DESeq2 with thresholds of $|\log_2(\text{fold change})| > 0.5$ and FDR < 0.05. For visualization and comparative analyses, biological replicates were merged and processed identically. Heatmaps and average profiles were generated using deepTools. Super-enhancers (SEs) were identified from H3K27ac ChIP-seq data using the ROSE algorithm [38] by ranking stitched enhancer regions based on signal intensity and defining SEs above the inflection point of the signal distribution curve. Differential SEs between DMSO- and Tm-treated cells were identified by constructing a union set of SE regions and comparing their activity using DESeq2 with the same thresholds as used for differential peak analysis. Motif enrichment analysis was performed on differential H3K27ac peaks using HOMER (v4.10). Motifs were identified using the findMotifsGenome.pl function with default parameters.

In situ Hi-C data processing

In situ Hi-C data were processed as previously described [28]. Briefly, paired-end reads were aligned to the human reference genome (hg19), and low-quality reads, singleton reads, self-ligated fragments, and other invalid read pairs were removed according to the HiC-Pro [39] (v2.11.4) filtering criteria. Valid interaction pairs were assigned to DpnII restriction fragments, and genome-wide contact matrices were generated at multiple resolutions. Biological replicates were assessed for reproducibility, and highly concordant datasets were merged and reprocessed to generate combined contact matrices for downstream analysis. Compartment analysis was performed using ICE-normalized Hi-C contact matrices at 100-kb resolution, and compartment transitions were identified using dcHiC (v2.1) [40] with a threshold of $P < .05$. Saddle plots were generated using cooltools (v0.7.1) [41]. Topologically associating domains (TADs) were identified using an insulation score-based approach, as described in a previous study [28]. Insulation scores were calculated, and TAD boundaries were determined based on the local minima of the insulation score profile.

HiChIP data processing

HiChIP data were processed as previously described [28], following the same pipeline as Hi-C data processing. Paired-end reads were aligned to the hg19 genome, and low-quality and invalid read pairs were filtered. Valid interaction pairs were assigned to DpnII restriction fragments. Chromatin loops were identified using FitHiChIP (v8.0) [42] in peak-to-all mode (IntType = 3), with a 5-kb bin size and interaction distances ranging from 10 kb to 2 Mb. Bias correction was applied using coverage normalization. Loops were identified with thresholds of $Q < 1 \times 10^{-5}$ for H3K27ac HiChIP and $Q < 0.01$ for ATF4 HiChIP. HiChIP loop anchors were annotated as promoter or enhancer anchors. Anchors overlapping promoter regions (defined as ± 2.5 kb from the transcription start sites of protein-coding genes) were classified as promoter anchors. Remaining anchors were classified as enhancer anchors if they overlapped H3K27ac ChIP-seq peaks, or as other anchors if no overlap was observed. A union set of loops detected across conditions was collected for differential loop analysis. Contact counts supporting each loop were quantified and compared using DESeq2, with differential loops defined by $|\log_2(\text{fold change})| > 0.5$ and $P < .05$.

Definition of TF target genes

TF target genes were defined as genes with TF binding at promoters or enhancers and showing decreased expression upon TF depletion. TF ChIP-seq peaks located within promoter regions or enhancers were identified in DMSO- and Tm-treated WT cells, with enhancer-associated binding restricted to enhancers connected to genes through HiChIP loops. Genes with TF peaks in their promoters and/or loop-connected enhancers were evaluated for expression changes in the corresponding TF knockout cells. Genes showing significantly decreased expression upon TF depletion $|\log_2(\text{fold change}) < -0.5$ and FDR $< 0.05|$ were defined as TF target genes.

TF peak overlap and co-binding analysis

To examine overlap among binding sites of the six TFs, ChIP-seq peaks from all TFs were combined, and all pairwise overlaps were computed using BEDtools (v2.25.0) [43] intersect, with overlap defined as genomic intervals sharing at least 1 bp. Overlap patterns were visualized using an UpSet plot generated with the ComplexUpset R package (v1.3.3). For detailed analysis of ATF4 and CHOP co-binding, TF peaks were classified into four categories. ATF4-only and CHOP-only peaks were identified using BEDtools -intersect with the −v option, and were defined as CHOP-less ATF4 and CHOP-only peaks, respectively. Peaks overlapping between ATF4 and CHOP were identified using BEDtools intersect and were classified as ATF4–CHOP shared peaks. To assess CHOP dependency of ATF4 binding, ATF4–CHOP shared peaks were further intersected with ATF4 peaks that were downregulated in CHOP knockout cells compared with WT cells. Shared peaks exhibiting reduced ATF4 binding upon CHOP depletion were defined as CHOP-dependent ATF4 peaks, whereas the remaining shared peaks were classified as CHOP-optional ATF4 peaks.

Functional validation of enhancers by CRISPR interference

To validate enhancer activity, a dCas9–KRAB-expressing HCT116 cell line was transduced with lentiviruses expressing enhancer-targeting gRNAs. gRNAs targeting ATF4-bound enhancers (Supplementary Table S4) were designed using TransCRISPR (v1.0) [44] to minimize off-target effects, and were cloned into the LentiGuide-Puro vector (Addgene, #52963). Lentiviruses were produced in 293FT cells by co-transfecting LentiGuide-Puro constructs with psPAX2 and pMD2.G plasmids (5.5 μg psPAX2, 0.7 μg pMD2.G, and 7.6 μg LentiGuide-Puro) and concentrated using Amicon filters

(Merck, UFC9010). Cells were infected with lentivirus at a multiplicity of infection of 0.5 in the presence of polybrene (8 μg ml^{-1}). After 16 h, the medium was replaced and cells were selected with puromycin (0.5 μg ml^{-1}) for 48 h, followed by Tm treatment for 6 h. Total RNA was extracted using RiboEx (GeneAll Biotechnology, 301-902) and reverse-transcribed for qPCR analysis.

Casilio-based imaging to quantify enhancer–promoter interactions

To investigate enhancer–promoter interactions at a representative locus, gRNAs targeting either the promoter or its associated enhancer (Supplementary Table S5) were designed using CHOPCHOP [45]. The promoter-targeting gRNA was cloned into the gRNA-20xPBS48107 vector (Addgene, #183215) and enhancer-targeting gRNAs were cloned into the gRNA-20xPBSc vector (Addgene, #183216) using BbsI digestion. Approximately 2×10^5 cells were seeded onto confocal dishes 24 h prior to transfection. Cells w re co-transfected with 750 ng of each gRNA vector, 100 ng PUF-mClover, and 100 ng PUF-iRFP670 using TurboFect (Thermo Fisher Scientific, R0531). The culture medium was replaced after 24 h, and cells were treated with Tm (0.5 μg ml^{-1}) for 6 h prior to imaging. Cells were stained with Hoechst 33342 (1 μg ml^{-1}) for 30 min at 37°C. Confocal imaging was performed 48 h after transfection using a Zeiss LSM 780 microscope equipped with a 100× oil-immersion objective. Z-stack images (10–15 μm total height, 0.37 μm step size) were acquired to capture the full nuclear volume. Images were analyzed using ZEN software (v3.8; Carl Zeiss). Z-stacks were processed by maximum-intensity projection, and the spatial proximity between promoter and enhancer loci was quantified by measuring the Euclidean distances between mClover and iRFP670 signals identified from three orthogonal views. Promoter–enhancer pairs within each nucleus were assigned based on the shortest inter-signal distance.

Flow cytometry-based amino acid uptake assay

Amino acid uptake capacity was assessed using an amino acid uptake assay kit (DOJINDO Laboratories, UP04-12). Cells were seeded in 24-well plates and treated with Tm (0.5 μg ml^{-1}) for 6 h prior to the assay. Boronophenylalanine (BPA) was used as an amino acid analog. After washing with Hank's balanced salt solution, cells were incubated with the probe solution according to the manufacturer's instructions. Stained cells were analyzed using flow cytometry with a FACSVerse system (BD Biosciences). All flow cytometry data collected by FACSuite (BD Biosciences) were analyzed using the FlowJo software (Treestar). Three biological replicates were performed for each condition.

Flow cytometry-based apoptosis assay

Apoptosis was assessed using an eBioscience™ Annexin V Apoptosis Detection Kit (Invitrogen, 88-8005-74) according to the manufacturer's instructions. Approximately 2×10^5 cells were treated with Tm (0.5 μg ml^{-1}) for 48 h prior to the assay. Cells were harvested, washed with phosphate-buffered saline, and resuspended in 1× binding buffer, followed by incubation with Annexin V–APC at room temperature for 10 min. After washing, cells were incubated with propidium iodide for 15 min at room temperature. Stained cells were analyzed using flow cytometry with a FACSVerse system (BD Biosciences). All flow cytometry data collected by FACSuite (BD Biosciences) were analyzed using FlowJo software (Treestar). Three biological replicates were performed for each condition.

Statistical analysis

All statistical analyses were performed using R (v4.4.1) and GraphPad Prism (v5.03). Statistical significance for qPCR analyses of individual genes, RNA-seq-based expression analyses, and Casilio imaging experiments was assessed using unpaired two-tailed Welch's *t*-test. Differences in expression changes of loop-connected genes were evaluated using the two-sided Wilcoxon rank-sum test. For amino acid transport and apoptosis assays involving multiple-group comparisons, statistical significance was determined using one-way analysis of variance (ANOVA) followed by Benjamini–Hochberg (BH) multiple-testing correction. Unless otherwise stated, data are presented as mean ± SEM. Significance levels are indicated as $P < .05$, $P < .01$, and $P < .001$.

Results

ER stress induces widespread enhancer activation and dynamic chromatin looping

To systematically investigate how ER stress reshapes transcriptional regulation, we performed integrated multi-omics analyses in WT cells under basal and ER stress conditions. Cells were treated with Tm for 6 h to induce ER stress, and RNA-seq, ATAC-seq, H3K27ac ChIP-seq, Hi-C, and H3K27ac HiChIP were performed to capture changes in gene expression, chromatin accessibility, enhancer activity, higher-order chromatin organization, and chromatin looping (Supplementary Fig. S1A). This treatment robustly induced canonical UPR TFs without affecting cell viability under the conditions used for subsequent analyses (Supplementary Fig. S1B–D).

RNA-seq analysis identified 1258 upregulated genes associated with protein homeostasis and ER stress responses and 1589 downregulated genes enriched for developmental and differentiation pathways (Fig. 1A and Supplementary Fig. S1E). Genes that were upregulated upon Tm treatment were hereafter defined as ESRGs. We performed ATAC-seq to assess whether these transcriptional changes were accompanied by broad changes in chromatin accessibility. Despite the widespread transcriptional response, ER stress induced only modest changes in chromatin accessibility, with 158 gained peaks and 65 lost peaks (Fig. 1B). In contrast, H3K27ac ChIP-seq revealed a marked increase in enhancer-associated activity, with 6253 gained peaks and 1115 lost peaks (Fig. 1C). Representative genomic tracks illustrated that transcriptional induction under ER stress was accompanied by pronounced increases in the H3K27ac signal, whereas changes in the ATAC-seq signal were comparatively limited (Fig. 1D). Consistent with this, gained H3K27ac peaks were predominantly located in enhancer-associated intergenic and intronic regions (Fig. 1E), where Tm-induced increases in H3K27ac levels were greater than those at promoters (Fig. 1F). Together, these results indicate that ER stress-induced transcriptional reprogramming is associated more strongly with enhancer activation than with widespread changes in chromatin accessibility.

We next asked whether ER stress alters higher-order chromatin organization. Hi-C analysis (Supplementary Fig. S1F)

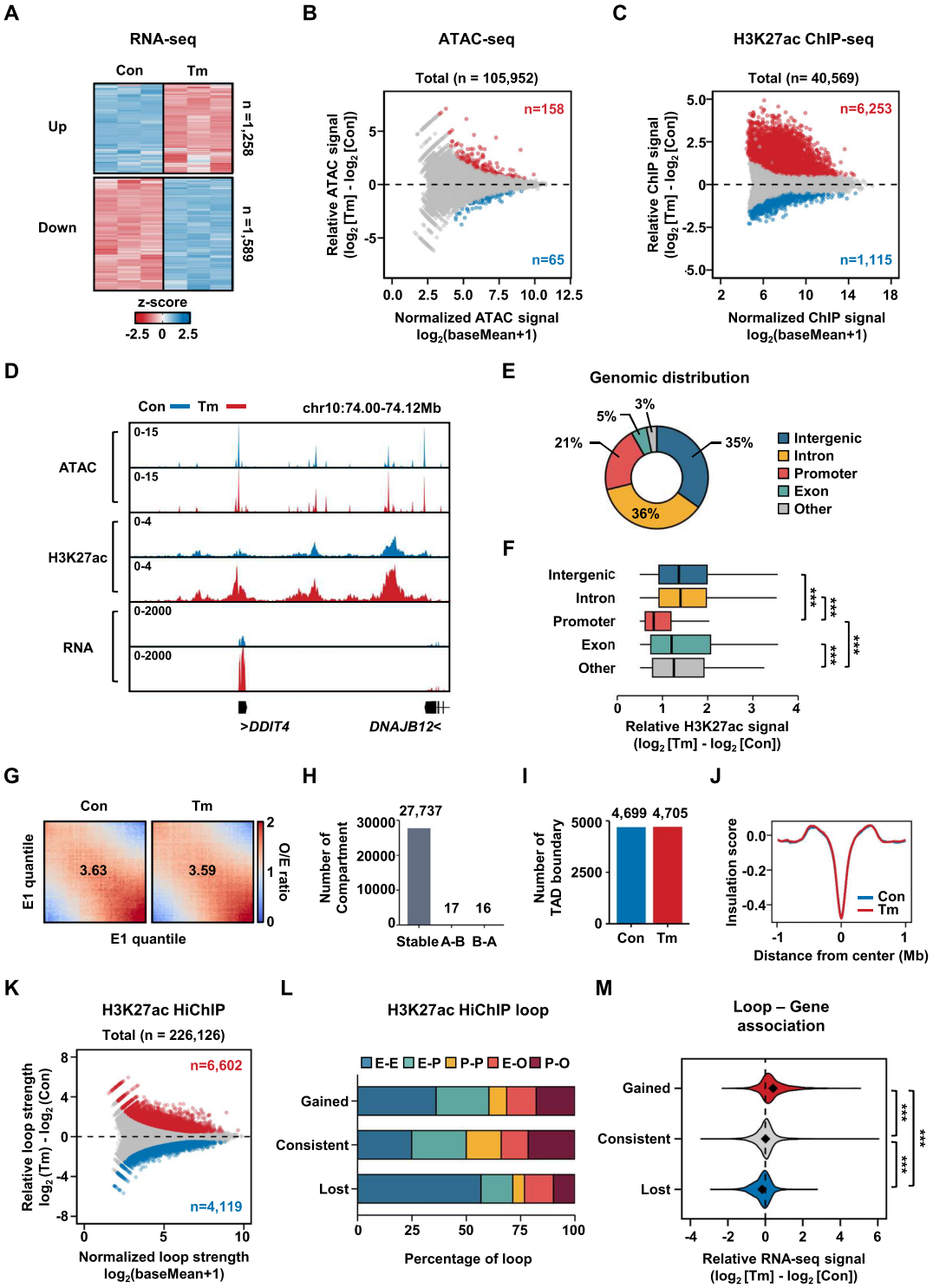

Figure 1. ER stress induces widespread enhancer activation and dynamic chromatin looping. (**A**) RNA-seq heatmap of differentially expressed genes (DEGs) in cells treated with 0.5 μg ml^{-1} Tm for 6 h ($n = 3$). Genes exhibiting differential expression (|log_2 fold change| > 0.5, FDR < 0.05) between control and Tm-treated cells are shown. Genes upregulated upon Tm treatment were hereafter defined as ESRGs. Gene expression levels were *z*-score normalized across samples. MA plots showing significant changes in ATAC-seq peak signal (**B**) or H3K27ac ChIP-seq peak signal (**C**) upon Tm treatment. The numbers of peaks showing differential signal (|log2 fold change| > 0.5, FDR < 0.05) in control (blue) or Tm-treated (red) cells are indicated. (**D**) Genome browser snapshot showing ATAC-seq, H3K27ac ChIP-seq, and RNA-seq signal tracks across a representative genomic region. (**E**) Genomic distribution of gained H3K27ac peaks upon Tm treatment. (**F**) Relative changes in H3K27ac levels across peak classes upon Tm treatment. (**G**) Saddle plots showing compartmentalization strength in control and Tm-treated cells. (**H**) A/B compartment switching upon Tm treatment. (**I**) Number of TAD boundaries identified in control and Tm-treated cells. (**J**) Genome-wide average insulation scores plotted as a function of distance from the TAD boundary centers defined in control cells. (**K**) MA plot showing significant changes in the H3K27ac HiChIP loop strength upon Tm treatment. The numbers of loops showing differential intensity (|log2 fold change| > 0.5, $P < .05$) in control (blue) or Tm-treated (red) cells are indicated. (**L**) Distribution of regulatory element classes at H3K27ac HiChIP loop anchors. E, enhancer; P, promoter; O, other. (**M**) Log_2 fold changes in RNA expression of genes associated with differential H3K27ac HiChIP loops.

revealed that compartment architecture was largely preserved, with only a small fraction of A/B compartments undergoing switching upon Tm treatment (Fig. 1G and H). A/B compartments represent large-scale chromatin domains broadly associated with active/open (A) or inactive/closed (B) genomic environments. Similarly, the number and insulation strength of TAD boundaries showed minimal differences between the control and ER stress conditions (Fig. 1I and J), indicating that ER stress does not substantially reorganize chromatin architecture at the compartment or TAD scale.

In contrast, H3K27ac HiChIP analysis, which enriches chromatin interactions associated with active regulatory elements marked by H3K27ac, revealed dynamic remodeling of chromatin looping under ER stress. We identified 6602 gained loops and 4119 lost loops following Tm treatment (Fig. 1K). Differential loops were predominantly anchored at regulatory elements, including enhancer–enhancer, enhancer–promoter, and promoter–promoter interactions (Fig. 1L). Moreover, genes associated with gained loops showed increased expression, whereas genes associated with lost loops tended to be downregulated (Fig. 1M). These observations suggest that ER stress-responsive transcription is accompanied by widespread enhancer activation and dynamic changes in chromatin looping, while chromatin accessibility and higher-order chromatin organization remain comparatively stable.

ER stress-responsive enhancers and chromatin loops are selectively associated with UPR TFs

To identify TFs associated with stress-induced enhancer remodeling, we first performed motif analysis on gained and lost H3K27ac peaks defined in WT cells. Motifs for AP-1 family members were enriched in both gained and lost peaks; whereas, motifs for ATF4, CHOP, C/EBPβ, and NFIL3 were selectively enriched in gained peaks (Fig. 2A). These motif patterns were accompanied by increased RNA expression of the corresponding TFs under ER stress (Fig. 2A), suggesting that selective activation of UPR-associated TFs may contribute to stress-induced enhancer activation.

To directly examine TF occupancy under ER stress, we performed ChIP-seq for six UPR-associated TFs: ATF4, CHOP, C/EBPβ, NFIL3, ATF6, and XBP1. Comparison of control and Tm-treated cells showed widespread binding changes across these six factors, with most factors exhibiting increased genomic occupancy under ER stress (Fig. 2B). Genomic distribution analysis further revealed distinct binding preferences among them. ATF4, CHOP, C/EBPβ, and NFIL3 showed substantial occupancy at distal regulatory regions, whereas ATF6 and XBP1 were more prominently enriched at promoter-proximal regions (Fig. 2B). Representative genome browser tracks illustrated these distinct binding patterns together with H3K27ac signal changes under ER stress (Fig. 2C).

We next examined how these TFs were distributed across differential H3K27ac peaks. Heatmap analysis showed that ATF4, CHOP, C/EBPβ, and NFIL3 were preferentially associated with enhancer-class H3K27ac peaks, whereas ATF6 and XBP1 showed stronger association with promoter-class peaks (Fig. 2D). To quantify the relationship between TF occupancy and enhancer activation, we compared TF ChIP-seq signal intensity with H3K27ac induction at the corresponding TF binding sites in WT cells. All six factors showed positive correlations to varying extents, with ATF4 exhibiting the strongest relationship with enhancer activation (Fig. 2E).

Because ER stress also induced dynamic chromatin looping, we next examined whether TF occupancy was similarly associated with loop remodeling. For loops anchored at TF ChIP-seq peaks, TF binding intensity positively correlated with stress-induced changes in H3K27ac HiChIP loop intensity, again with ATF4 showing the strongest association (Fig. 2F). Together, these analyses indicate that stress-responsive enhancers and chromatin loops are not uniformly associated with all UPR TFs, but instead show selective engagement of distinct TF classes. In particular, enhancer-associated factors such as ATF4, CHOP, and C/EBPβ are preferentially linked to stress-induced enhancer activation and chromatin looping, whereas ATF6 and XBP1 are more strongly associated with promoter-proximal regulation.

UPR TFs regulate ER stress gene programs via enhancers and promoters

Having identified selective associations between UPR TFs and stress-responsive enhancers and chromatin loops, we next sought to define their direct target genes in a comprehensive and mechanistically informed manner. Knockout cell lines for all six UPR-associated TFs were generated and validated by genomic PCR and immunoblot analysis (Supplementary Fig. S2), followed by RNA-seq, H3K27ac ChIP-seq, TF ChIP-seq, and H3K27ac HiChIP to define the regulatory functions of each factor (Supplementary Fig. S3). As an initial measure of transcriptional dependence, we quantified the numbers of downregulated DEGs in each of the six TF knockout cell lines under control and ER stress conditions. All six knockout lines showed reduced expression of distinct gene sets, and the number of downregulated DEGs generally increased upon Tm treatment (Fig. 3A), indicating that ER stress broadens the transcriptional programs dependent on these factors.

To distinguish direct regulatory effects from secondary transcriptional changes, we next applied an integrative framework combining TF ChIP-seq, H3K27ac HiChIP, and RNA-seq datasets from the corresponding TF knockout cells (Fig. 3B). Genes were classified as direct targets if they met both of the following criteria: (i) the presence of a TF ChIP-seq peak within a promoter or enhancer associated with the gene; and (ii) reduced RNA expression in the corresponding TF knockout cells relative to WT controls under DMSO or Tm treatment conditions. This strategy allowed us to define direct target genes based on both regulatory occupancy and transcriptional dependency (Supplementary Fig. S4 and Supplementary Tables S6–S11). Representative examples of direct target genes illustrating promoter-associated, enhancer-associated, or mixed regulatory configurations for each TF are shown in Supplementary Fig. S5.

Using this framework, we identified distinct sets of direct target genes for each of the six TFs under basal and ER stress conditions (Fig. 3C). Under basal conditions, CHOP and XBP1 regulated relatively few direct targets, whereas the remaining TFs controlled larger gene sets. Upon Tm treatment, the numbers of direct target genes increased markedly for all six factors, indicating broad expansion of TF-mediated regulatory programs during ER stress.

We next asked how extensively these TF target genes account for ER stress-responsive transcription. Intersection of the union of all six TF direct target gene sets with ESRGs showed that 44% of ESRGs overlapped with at least one TF target set (Fig. 3D). We refer to these overlapping genes

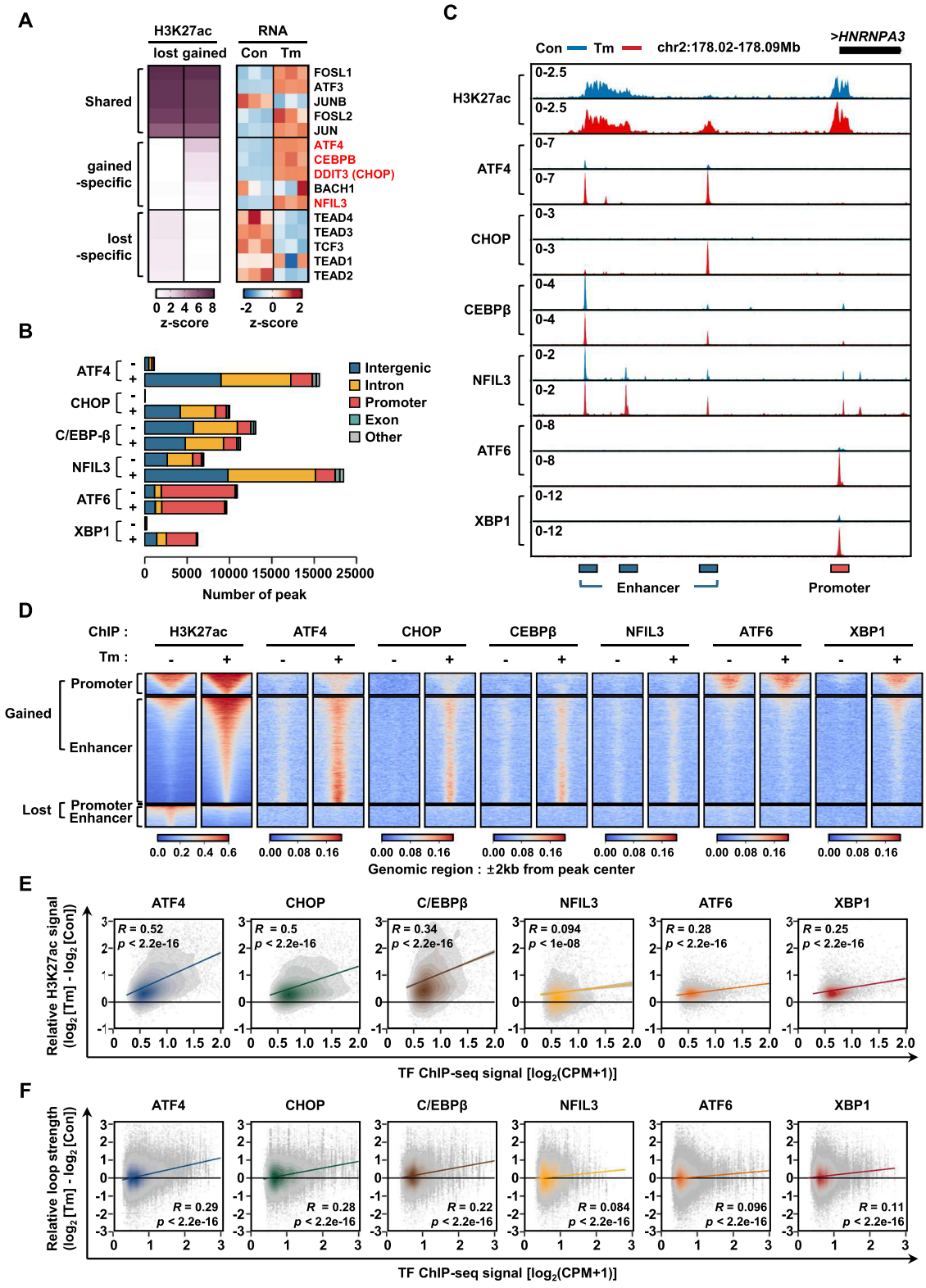

Figure 2. UPR TFs selectively associate with ER stress-responsive enhancers and chromatin loops. (**A**) Heatmap showing motif enrichment in gained and lost H3K27ac peaks together with RNA expression changes of the corresponding TFs. The top five motifs enriched in shared, gained, or lost peaks are shown. (**B**) Numbers and genomic distribution of ChIP-seq peaks for the six TFs in control and Tm-treated cells. (**C**) Representative genome browser tracks showing ChIP-seq signals for six TFs and H3K27ac in control and Tm-treated cells. (**D**) Heatmap of ChIP-seq signal intensities for six TFs across differential H3K27ac peaks, stratified into promoter and enhancer regions. (**E**) Correlation between TF binding intensity and changes in enhancer activity during ER stress in WT cells. TF binding intensity was quantified as $\log_2(\text{CPM} + 1)$ at TF ChIP-seq peaks in Tm-treated WT cells, and enhancer activity changes were calculated as $\log_2(\text{Tm}) - \log_2(\text{Con})$ of the H3K27ac signal at the corresponding peaks. (**F**) Correlation between TF binding intensity and changes in chromatin loop intensity during ER stress in WT cells. TF binding intensity was quantified as $\log_2(\text{CPM} + 1)$ at TF ChIP-seq peaks in Tm-treated WT cells, and loop changes were calculated as $\log_2(\text{Tm}) - \log_2(\text{Con})$ of the H3K27ac HiChIP loop intensity for loops anchored at the corresponding peaks.

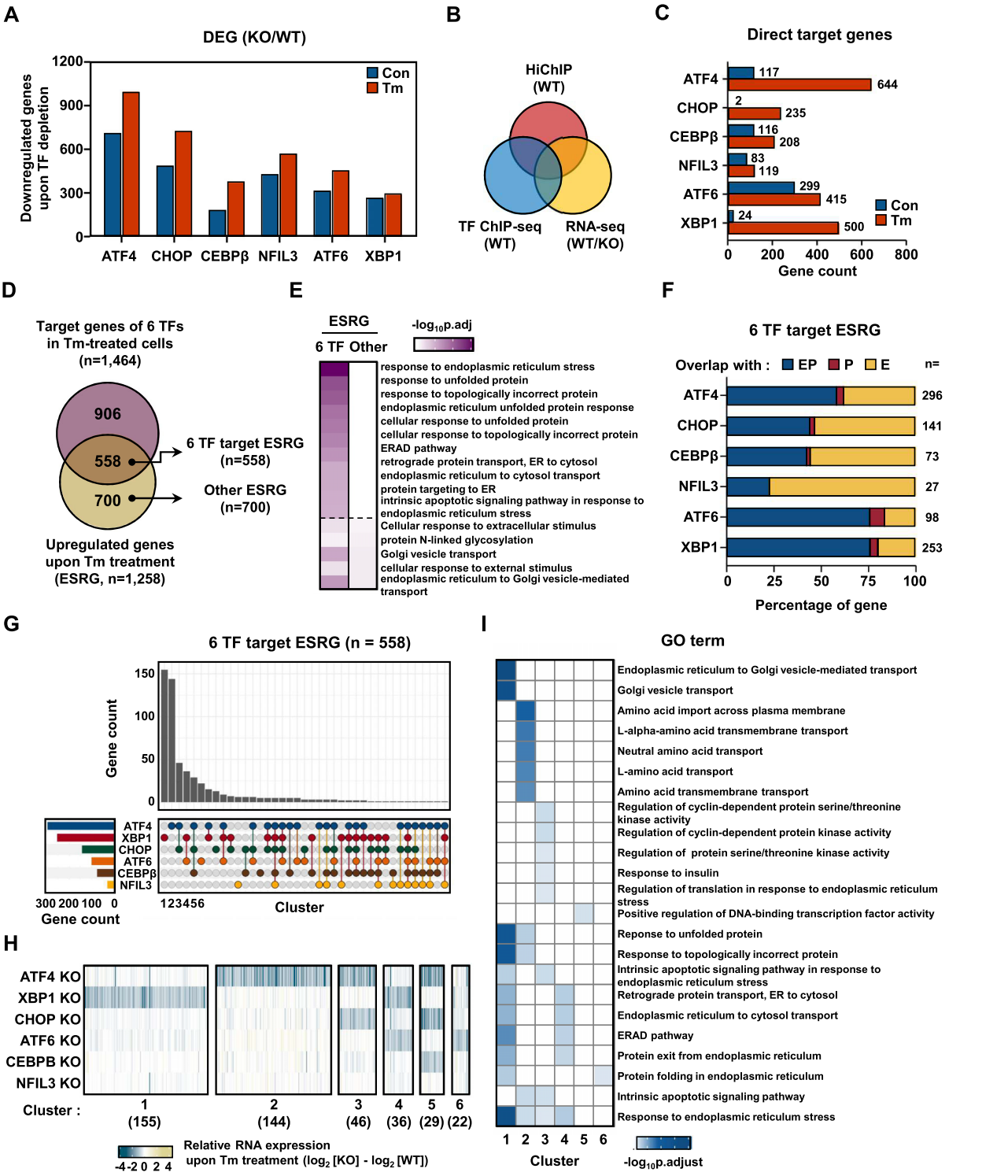

Figure 3. Integrative multi-omics identification of direct target genes of UPR TFs. (**A**) Numbers of downregulated genes identified by RNA-seq upon TF depletion under control (DMSO) and Tm treatment conditions. (**B**) Schematic overview of the integrative strategy used to define direct target genes of UPR TFs. Direct targets were identified by combining TF ChIP-seq, H3K27ac HiChIP, and RNA-seq data. Genes were classified as direct targets if they met both of the following criteria: (i) presence of a TF ChIP-seq peak within a promoter or enhancer associated with the gene; and (ii) reduced RNA expression in the corresponding TF knockout cells relative to WT cells under DMSO or Tm treatment conditions. (**C**) Numbers of direct target genes identified for the six TFs under control (DMSO) and Tm treatment conditions. (**D**) Overlap between direct target genes of the six TFs and ESRGs. ESRGs overlapping with any of the six TF target gene sets are referred to as "six TF target ESRGs," and non-overlapping ESRGs are classified as "other ESRGs." (**E**) GO enrichment analysis of six TF target ESRGs and other ESRGs. (**F**) Numbers of six TF target ESRGs categorized by the genomic location of associated TF ChIP-seq peaks. E, enhancer; P, promoter; EP, both enhancer and promoter. (**G**) UpSet plot showing combinatorial overlap among TF target genes that are upregulated upon Tm treatment. The upper bar plot indicates the number of Tm-upregulated TF target genes (ESRGs) corresponding to each TF combination shown below, and the left bar plot indicates the total number of Tm-upregulated TF target genes for each TF, rather than the total TF target gene counts shown in panel (C). (**H**) Heatmap showing RNA expression changes of genes belonging to the top six combinatorial TF target gene groups in TF knockout cells relative to WT cells. (**I**) GO enrichment analysis of genes in the top six combinatorial TF target gene groups.

as "six-TF target ESRGs," whereas non-overlapping ESRGs were classified as "other ESRGs." GO analysis revealed clear functional differences between these two groups. Six TF target ESRGs were strongly enriched for canonical ER stress pathways, including UPR, ER-associated degradation (ERAD), and related proteostasis programs, whereas other ESRGs were associated more broadly with general protein homeostasis processes (Fig. 3E). These findings indicate that a substantial fraction of the core ER stress transcriptional response is directly controlled by the six UPR-associated TFs.

We next examined how these TFs regulate their direct targets with respect to genomic regulatory architecture. Classification of six TF target ESRGs according to the locations of the associated TF ChIP-seq peaks revealed distinct regulatory modes among the six factors. ATF4, CHOP, C/EBPβ, and NFIL3 predominantly regulated genes through enhancer-associated binding, whereas ATF6 and XBP1 showed a stronger promoter-biased pattern (Fig. 3F). This distinction is consistent with the occupancy patterns observed in Fig. 2B, and suggests that UPR TFs engage stress-responsive gene expression through different regulatory strategies.

Because many stress-responsive genes were associated with more than one TF, we next examined the extent of combinatorial control among direct target genes. UpSet analysis revealed that, although some genes were uniquely regulated by individual factors, a substantial fraction was shared by multiple TFs (Fig. 3G). The numbers shown in Fig. 3G represent the subset of TF target genes that are upregulated upon Tm treatment, i.e. ESRGs, rather than the total TF target gene counts shown in Fig. 3C. The most prominent combinatorial groups included both TF-specific and shared target sets, such as ATF4-specific, XBP1-specific, ATF4–CHOP, and ATF6–XBP1 groups. Heatmap analysis of the top six combinatorial TF target groups showed distinct expression dependencies across TF knockout lines (Fig. 3H), indicating that these genes are governed by characteristic patterns of combinatorial regulation rather than by simple one-factor control. GO analysis further showed that these groups were associated with both shared and TF-selective biological functions (Fig. 3I). Core ER stress pathways, including UPR, ERAD, and apoptosis-related programs, were enriched across multiple TF combinations; whereas, other processes were more selectively associated with particular TF groups.

Together, these results define a comprehensive set of direct target genes for six UPR-associated TFs and show that ESRG expression is regulated through both enhancer- and promoter-based mechanisms, with extensive combinatorial control across the transcriptional network.

ATF4 is a dominant regulator of enhancer activation and chromatin looping during ER stress

Given that multiple UPR TFs contribute to ESRG regulation, we next compared their relative contributions to enhancer activation and chromatin looping. As shown in Fig. 2E, TF-binding intensity positively correlated with Tm-induced H3K27ac changes for most factors in WT cells. However, knockout analyses revealed a clear functional hierarchy. NFIL3 knockout had minimal effects; whereas, loss of ATF6, C/EBPβ, XBP1, or CHOP caused partial reductions in H3K27ac at enhancers gained upon Tm treatment in WT cells. In contrast, ATF4 depletion produced the most pronounced decrease in Tm-induced H3K27ac across gained enhancers, indicating that ATF4 plays a dominant role in enhancer activation (Fig. 4A). A similar hierarchy was observed for chromatin looping. In WT cells, TF binding intensity positively correlated with stress-induced changes in loop intensity at loops anchored by TF ChIP-seq peaks (Fig. 2F). Again, ATF4 loss caused the strongest reduction in Tm-induced loop intensity, whereas loss of the other factors had only partial or minimal effects (Fig. 4B). Together, these findings establish ATF4 as the dominant regulator of stress-induced enhancer activation and chromatin looping.

We next asked whether this hierarchy extends to SE regulation. Ranked H3K27ac signal plots revealed widespread remodeling of the SE landscape upon Tm treatment, with 88 gained SEs and 17 lost SEs (Supplementary Fig. S6A and B). H3K27ac density profiles confirmed strong activation of gained SEs and reduction of lost SEs under ER stress (Supplementary Fig. S6C). Analysis of Tm-upregulated SEs defined in WT cells showed that depletion of most factors caused minimal or partial effects, whereas ATF4 loss led to a pronounced and global reduction in the H3K27ac signal across stress-induced SEs (Fig. 4C). Together, these findings extended the dominant role of ATF4 from enhancer activation and chromatin looping to SE regulation during ER stress.

ATF4-dependent enhancers regulate transcription through long-range chromatin interactions

Given that ATF4 emerged as a dominant regulator of enhancer activation and chromatin looping during ER stress, we next asked whether ATF4-dependent enhancers directly control transcription through long-range chromatin interactions. To address this question, we focused on *BBS10* as a representative ER stress-responsive locus linked to a distal ATF4-bound enhancer located far from its promoter (Fig. 5A). *BBS10* encodes a chaperonin-like protein required for cilia formation [46, 47].

In WT cells, Tm treatment markedly increased ATF4 occupancy primarily at a distal enhancer located ∼685 kb upstream of the *BBS10* promoter, while ATF4 binding at the promoter was minimal. Tm treatment also increased the H3K27ac levels at this enhancer and strengthened enhancer–promoter contacts (Fig. 5A). In ATF4-knockout cells, these Tm-induced changes were abolished, indicating that enhancer activation and long-range chromatin looping at the *BBS10* locus are ATF4-dependent.

To independently validate ER stress-induced enhancer–promoter proximity at the *BBS10* locus, we employed a Casilio-based imaging strategy [48] that labeled the *BBS10* promoter with Clover and the distal ATF4-bound enhancer with RFP (Fig. 5B). Confocal imaging revealed that Tm treatment significantly reduced the spatial distance between the enhancer and promoter in WT cells, consistent with the loop formation under ER stress (Fig. 5C and D). This reduction in enhancer–promoter distance was not observed in ATF4-knockout cells, further supporting an essential role for ATF4 in mediating long-range chromatin interactions at this locus. Consistent with these structural changes, *BBS10* expression was robustly induced by Tm in WT cells but was markedly attenuated in ATF4-knockout cells (Fig. 5E). Together, these findings indicate that ATF4-dependent enhancer activation can be functionally coupled to long-range chromatin interactions and transcriptional induction during ER stress.

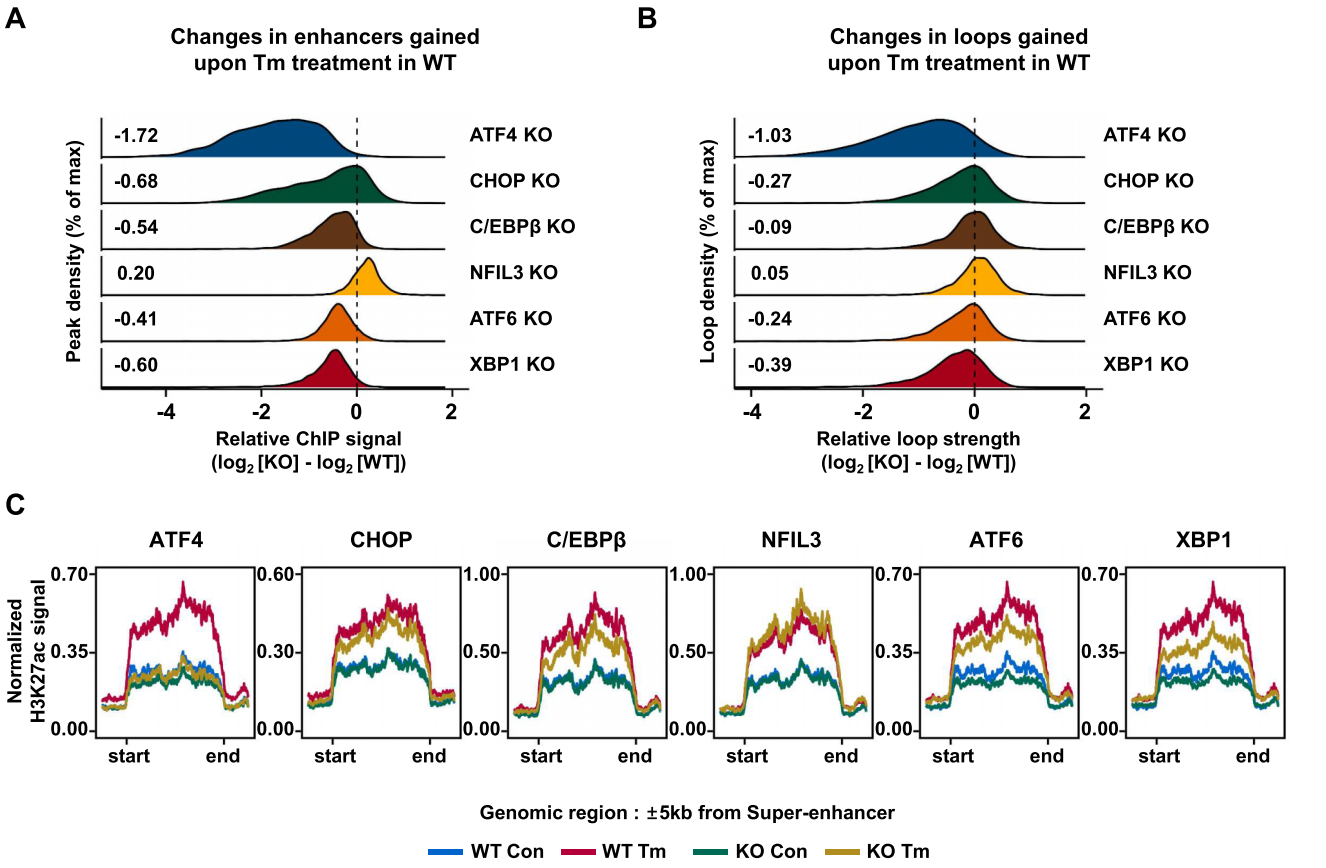

Figure 4. ATF4 is a dominant regulator of enhancer activation, chromatin looping, and SE activation during ER stress. (**A**) Density plots of H3K27ac signal changes in TF KO cells relative to WT cells at peaks induced by Tm treatment in WT cells. (**B**) Density plots of loop strength changes in TF KO cells relative to WT cells at loops induced by Tm treatment in WT cells. (**C**) H3K27ac ChIP-seq line plots centered on WT-defined Tm-upregulated SEs in WT control, WT Tm, KO control, and KO Tm conditions across the six TF KO lines.

We next examined the *VEGFA–GTPBP2* region as an additional example of ATF4-dependent long-range enhancer regulation. At this locus, Tm treatment increased ATF4 occupancy and H3K27ac at a distal enhancer, strengthened H3K27ac HiChIP interactions, and induced expression of both *VEGFA* and *GTPBP2* in WT cells (Supplementary Fig. S7A). These Tm-induced changes were largely absent in ATF4-knockout cells: enhancer activation was abolished (Supplementary Fig. S7A), and induction of *VEGFA* and *GTPBP2* expression was almost completely lost (Supplementary Fig. S7B). Consistent with this, CRISPR interference targeting the distal enhancer significantly reduced Tm-induced expression of both genes (Supplementary Fig. S7C). Notably, this enhancer was linked to the regulation of two target genes, *VEGFA* and *GTPBP2*, suggesting that ATF4-associated distal enhancers can support coordinated regulation of multiple nearby genes during ER stress.

We further examined the DDIT4 locus as an additional example of ATF4-dependent long-range enhancer regulation. Similar to the *BBS10* and *VEGFA–GTPBP2* loci, Tm treatment increased ATF4 occupancy and H3K27ac at a distal enhancer, strengthened H3K27ac HiChIP interactions, and induced DDIT4 expression in WT cells (Supplementary Fig. S8A). These stress-induced changes were markedly attenuated by ATF4 depletion and by CRISPR interference targeting the distal enhancer, indicating that ATF4-dependent enhancer activation and long-range chromatin interactions contribute to transcriptional regulation at the DDIT4 locus (Supplementary Fig. S8B and C).

Together, these results demonstrate that ATF4-dependent enhancer activation is coupled to long-range chromatin interactions and transcriptional induction, establishing a direct link between distal enhancer regulation and ESRG expression.

CHOP modulates ATF4 binding to selectively regulate enhancer activation during ER stress

Although ATF4 broadly associates with stress-induced enhancer activation and chromatin looping, our analyses indicated that many ESRGs are co-regulated by multiple TFs (Fig. 3G and H). We therefore asked how such combinatorial regulation is implemented at individual genomic loci. Because all six TFs analyzed in this study belong to the bZIP family and can form homo- or heterodimers in a context-dependent manner [18–21], we investigated whether specific bZIP partners influence ATF4 DNA binding during ER stress.

Pairwise overlap analysis of TF ChIP-seq peaks revealed that ATF4 most extensively co-occupied genomic regions with CHOP, followed by C/EBPβ, NFIL3, XBP1, and ATF6 (Fig. 6A). Notably, ATF4–CHOP co-bound regions represented the most abundant pairwise overlap among all TF combinations, whereas ATF6 and XBP1 showed the strongest mutual overlap with each other. Because pairwise overlaps were assessed independently for each TF pair, individual genomic

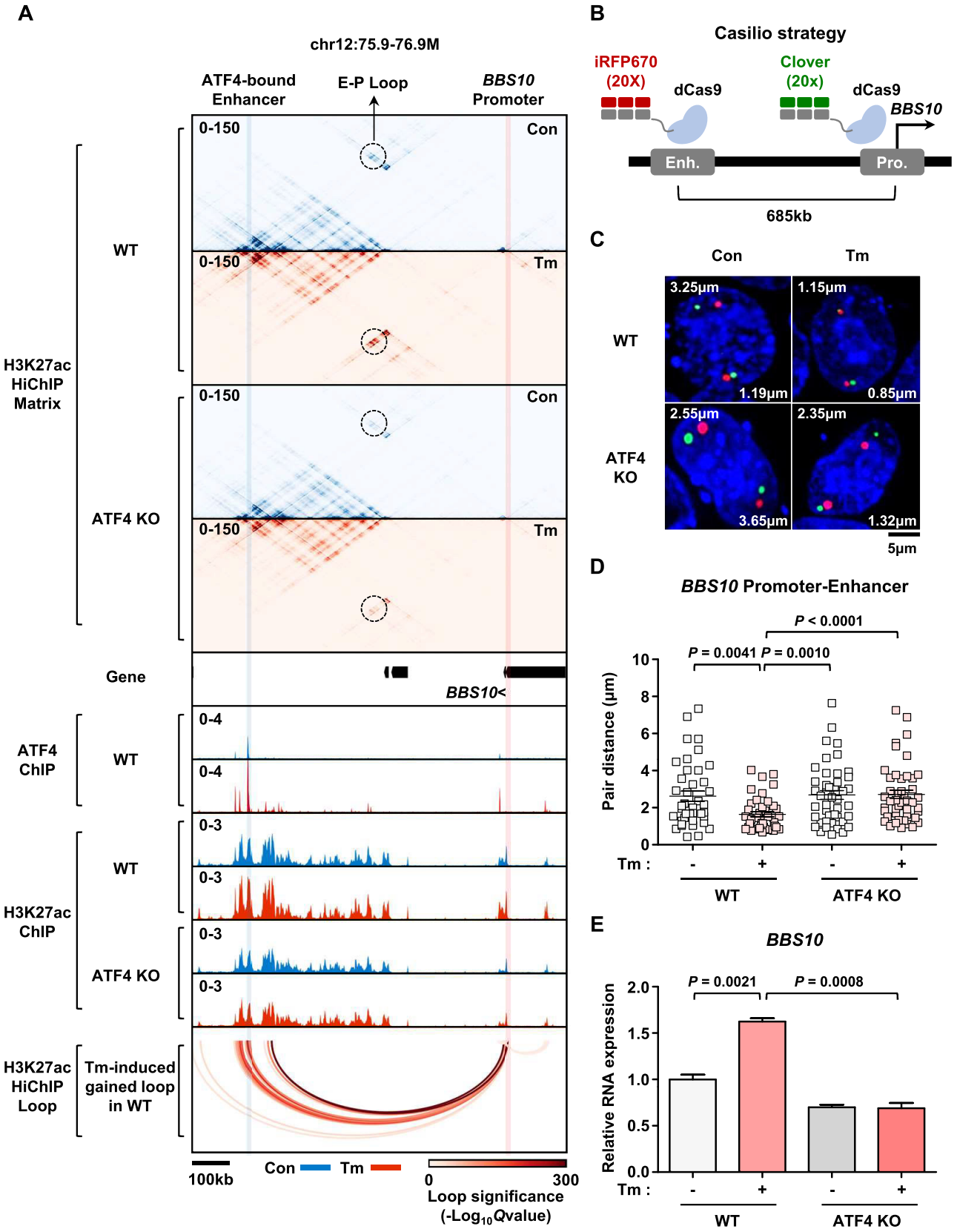

Figure 5. ATF4-dependent enhancers regulate transcription through long-range chromatin interactions at the *BBS10* locus. (**A**) Genome browser view showing strengthened chromatin contacts between an ATF4-bound distal enhancer and the *BBS10* promoter upon Tm treatment in WT cells and the loss of these interactions in ATF4-knockout cells. Tracks include the H3K27ac HiChIP contact matrix, ATF4 ChIP-seq signal, H3K27ac ChIP-seq signal, and H3K27ac HiChIP loops gained upon Tm treatment in WT cells. (**B**) Schematic illustration of the Casilio-based imaging strategy used to visualize enhancer–promoter interactions at the *BBS10* locus. (**C**) Representative confocal microscopy images showing spatial proximity between the ATF4-bound enhancer and the *BBS10* promoter in DMSO- and Tm-treated WT and ATF4-knockout cells. (**D**) Quantification of the pairwise distance between fluorescent foci corresponding to the ATF4-bound enhancer and the *BBS10* promoter in WT and ATF4-knockout cells under DMSO and Tm treatment conditions. (**E**) RNA expression levels of *BBS10* in DMSO- and Tm-treated WT cells and ATF4-knockout cells.

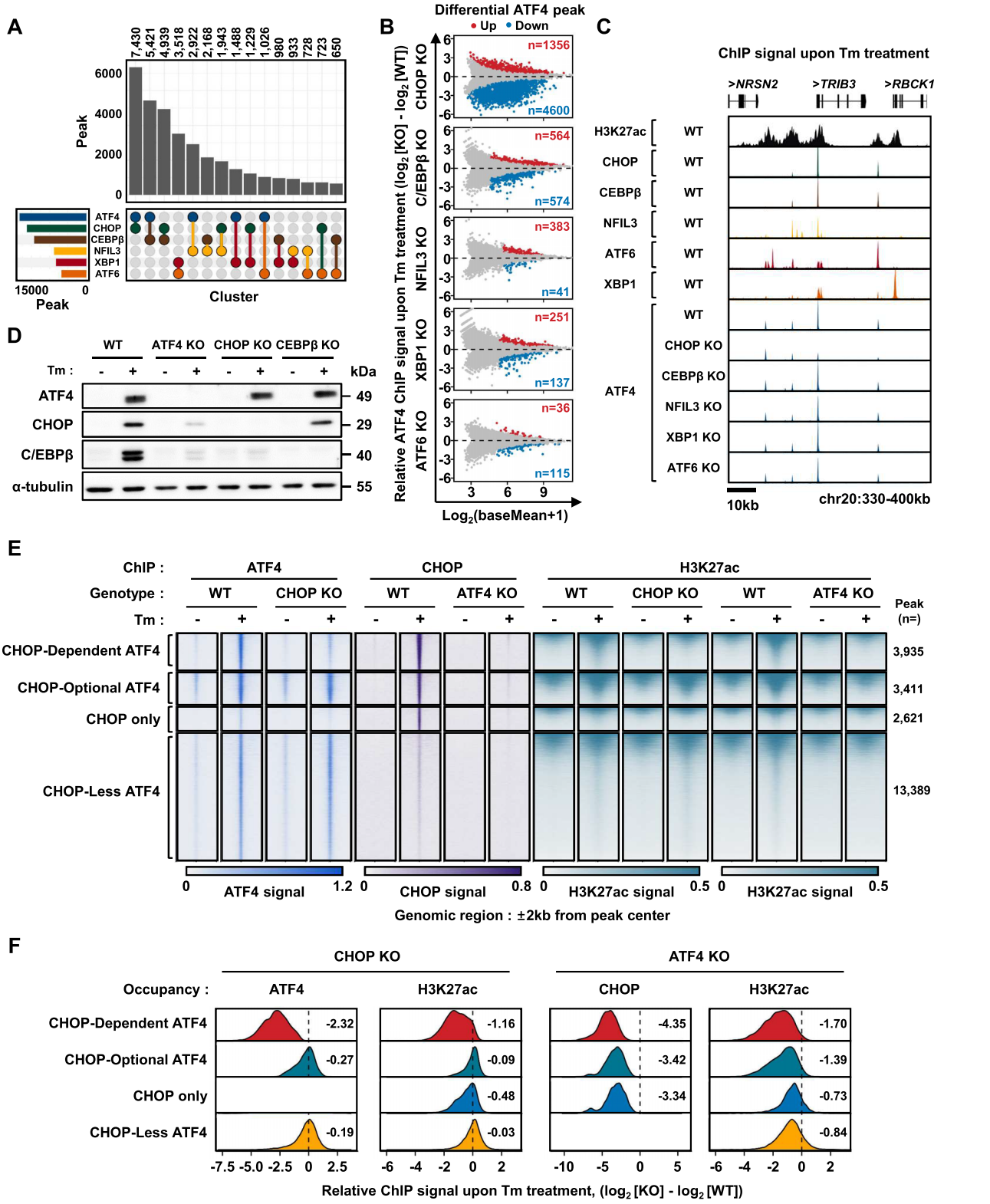

Figure 6. CHOP modulates ATF4 binding to selectively regulate enhancer activation during ER stress. (**A**) UpSet plot showing pairwise overlaps among ChIP-seq peaks of the six TFs in Tm-treated cells. Each set represents peaks shared between a given pair of TFs. Because overlaps were defined independently for each TF pair, individual genomic regions may have been included in multiple pairwise combinations. (**B**) Differential ATF4 ChIP-seq peak analysis comparing Tm-treated WT cells with the indicated TF-knockout cells. (**C**) Representative genomic example showing differential ATF4 binding at the *TRIB3* locus in Tm-treated WT and TF-knockout cells. (**D**) Protein levels of TFs in WT and TF-knockout cells, measured by western blotting. (**E**) Schematic classification of ATF4- and CHOP-bound regions in Tm-treated cells into four categories based on peak overlap and CHOP dependency of ATF4 binding, together with H3K27ac ChIP-seq signal intensities at the corresponding regions in DMSO- or Tm-treated WT, ATF4-knockout, and CHOP-knockout cells. (**F**) Density plots showing relative ATF4 occupancy (first panel) and H3K27ac levels (second panel) in CHOP-knockout cells compared with WT cells upon Tm treatment, and relative CHOP occupancy (third panel) and H3K27ac levels (fourth panel) in ATF4-knockout cells compared with WT cells upon Tm treatment.

regions could be included in multiple TF pair combinations. Nevertheless, the overall pattern was consistent with preferential co-occupancy of ATF4 and CHOP under ER stress.

To determine whether this co-occupancy reflects functional cooperation, we next assessed the effects of individual TF knockouts on ATF4 genomic occupancy. Comparison of ATF4 ChIP-seq peaks in Tm-treated WT and TF-knockout cells showed that knockout of C/EBPβ, NFIL3, XBP1, or ATF6 caused relatively modest changes in ATF4 binding, whereas CHOP knockout led to widespread differential ATF4 occupancy (Fig. 6B). A representative example at the *TRIB3* locus illustrated a strong reduction in ATF4 binding in CHOP-knockout cells compared with WT cells, whereas loss of the other TFs had substantially weaker effects (Fig. 6C). Importantly, immunoblot analysis confirmed that CHOP depletion did not substantially alter ATF4 protein abundance, indicating that the observed changes in ATF4 occupancy were not simply caused by altered ATF4 expression (Fig. 6D). Together, these results identify CHOP as the strongest modulator of ATF4 genomic occupancy among the six UPR-associated TFs.

To further define how CHOP influences ATF4 occupancy, we classified ATF4- and CHOP-bound regions in Tm-treated cells according to peak overlap and CHOP dependency of ATF4 binding. This analysis separated genomic regions into four categories—CHOP-dependent ATF4, CHOP-optional ATF4, CHOP-only, and CHOP-less ATF4 sites (Fig. 6E and Supplementary Fig. S9A)—and representative loci illustrated the close overlap of ATF4 and CHOP peaks at Tm-induced regulatory regions (Supplementary Fig. S9B). Because CHOP expression itself is regulated by ATF4, CHOP binding changes in ATF4-knockout cells were not used in this classification.

We next asked how these occupancy patterns relate to enhancer activation. Tm treatment induced a global increase in H3K27ac at ATF4-bound regions in WT cells, and this increase was largely abolished in ATF4-knockout cells (Fig. 6E and F). In contrast, CHOP knockout selectively reduced H3K27ac at CHOP-dependent ATF4 sites, with much weaker effects at CHOP-optional and CHOP-less ATF4 regions (Fig. 6E and F). These results support a model in which CHOP does not globally regulate ATF4-associated enhancers, but instead modulates enhancer activity at a distinct subset of ATF4-bound loci.

To test whether DNA sequence alone could explain this functional divergence, we performed motif analysis of ATF4 ChIP-seq peaks using MEME-STREME [49]. The CARE motif was enriched across ATF4-bound regions, and modest sequence variation was observed within the CARE consensus (Supplementary Fig. S9C). Additional analysis of flanking CARE motif variation and motif enrichment among non-canonical CARE peaks did not identify sequence features that clearly distinguished CHOP-dependent from CHOP-optional ATF4 peaks. Together, these results indicate that sequence features alone were insufficient to fully account for the differential CHOP dependency of ATF4 binding, suggesting that additional factors, such as chromatin context or local regulatory architecture, contribute to selective ATF4–CHOP cooperation.

Collectively, these results demonstrate that CHOP modulates ATF4 DNA binding and selectively regulates enhancer activation at a subset of stress-responsive regulatory elements, thereby providing a mechanistic basis for combinatorial transcriptional regulation during ER stress.

CHOP diversifies ATF4-dependent transcriptional programs during ER stress

Given that CHOP selectively modulates ATF4-dependent enhancer activation, we next asked how this interaction influences ATF4-driven transcriptional programs. To address this, we intersected ATF4 direct targets with ESRGs and defined the overlapping genes as ATF4 ESRGs (Fig. 7A). We then classified these ATF4 ESRGs according to whether their associated regulatory elements contained CHOP-dependent ATF4 peaks. Based on this criterion, ATF4 ESRGs were divided into two groups: CHOP-dependent ATF4 ESRGs, which contain CHOP-dependent ATF4 peaks in their associated promoters or enhancers; and CHOP-independent ATF4 ESRGs, which lack such peaks (Fig. 7B).

Among the 296 ATF4 ESRGs identified under ER stress conditions, 186 were classified as CHOP-dependent and 110 as CHOP-independent (Fig. 7B). We next examined how these two groups respond to loss of ATF4 or CHOP. In WT cells, both groups were robustly induced by Tm treatment (Fig. 7C and D). As expected, expression of both groups was markedly reduced in ATF4-knockout cells, confirming their broad dependence on ATF4 for stress-induced activation. In contrast, the two groups showed distinct responses to CHOP loss. Expression of CHOP-independent ATF4 ESRGs was largely preserved in CHOP-knockout cells, whereas expression of CHOP-dependent ATF4 ESRGs was significantly reduced (Fig. 7C and D). These data indicate that CHOP is not uniformly required for ATF4-driven transcription, but instead selectively supports a subset of ATF4-dependent stress-responsive genes.

Closer inspection further revealed that ATF4 ESRGs classified as CHOP-dependent exhibited heterogeneous responses to CHOP depletion, which gave rise to the apparent two groups in Fig. 7C. Importantly, this classification was based on the presence of at least one CHOP-dependent ATF4 peak at either the promoter or a loop-connected enhancer, whereas transcriptional sensitivity to CHOP depletion was evaluated separately based on gene expression changes in CHOP-knockout cells. Of the 186 CHOP-dependent ATF4 ESRGs, 92 were classified as CHOP-sensitive and 94 as CHOP-insensitive (Supplementary Fig. S10A and Supplementary Table S12). Individual genes could contain both CHOP-dependent and CHOP-independent ATF4 peaks, and their overall transcriptional output is therefore likely influenced by the combined contribution of these distinct regulatory elements. Consistent with this interpretation, CHOP-insensitive genes contained a significantly greater number of CHOP-independent ATF4 peaks than CHOP-sensitive genes (Supplementary Fig. S10B). In addition, CHOP-dependent ATF4 peaks showed significantly greater binding intensity in CHOP-sensitive genes than in CHOP-insensitive genes, whereas CHOP-independent peak intensity did not differ significantly between the two groups (Supplementary Fig. S10C). Together, these findings suggest that CHOP-dependent ATF4 ESRGs represent a continuum of CHOP dependency, rather than two discrete classes, shaped by both the abundance of CHOP-independent regulatory inputs and the relative strength of CHOP-dependent ATF4 binding.

Representative examples further illustrated these distinct regulatory patterns (Fig. 7E and F). Genes classified as CHOP-dependent ATF4 ESRGs showed strong stress-induced expression in WT cells but markedly reduced induction in both ATF4- and CHOP-knockout cells. In contrast,

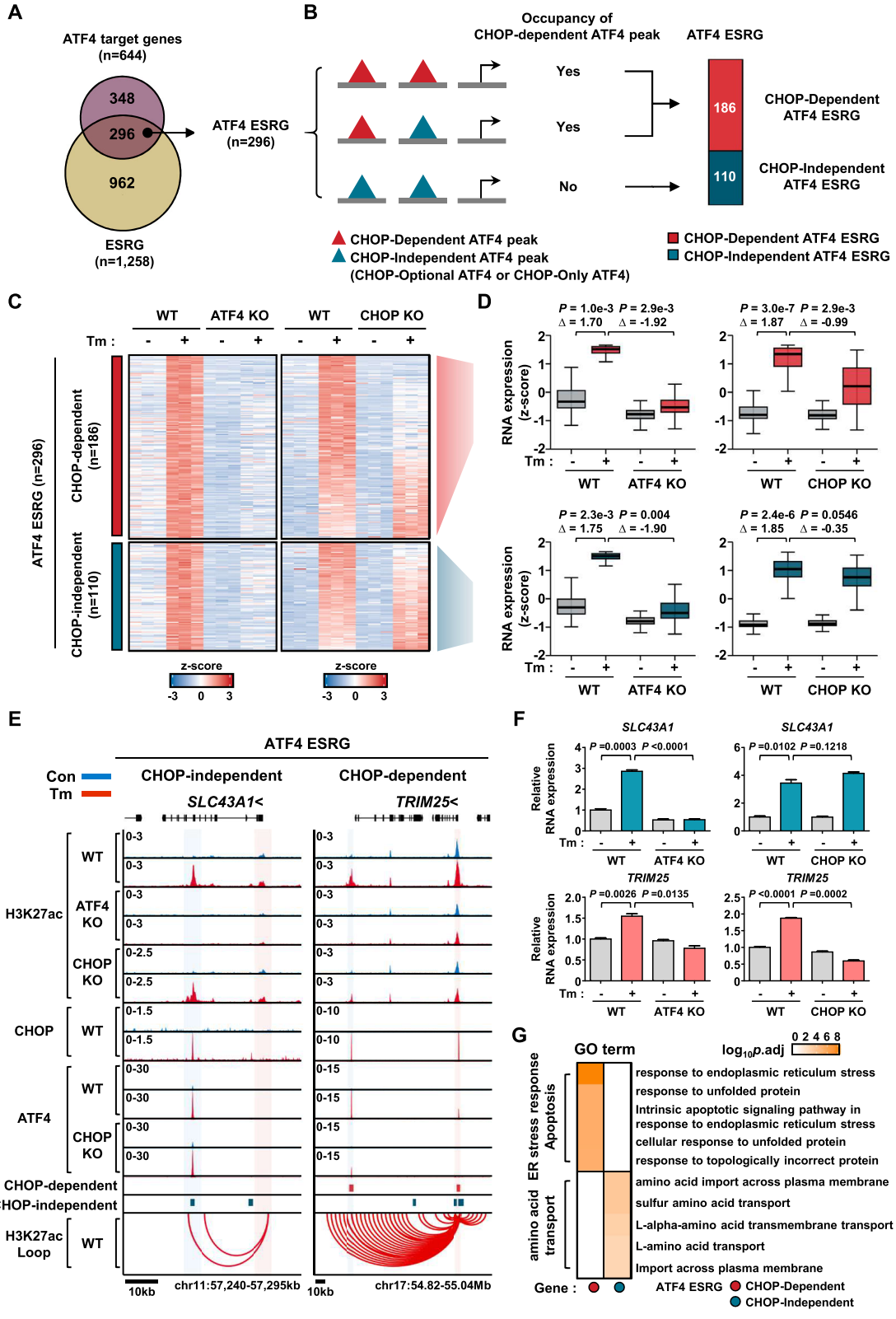

Figure 7. CHOP diversifies ATF4-dependent transcriptional programs during ER stress. (**A**) Overlap between ATF4 direct target genes and ESRGs. Genes shared by both groups are defined as ATF4 ESRGs. (**B**) Classification of ATF4 ESRGs based on the presence of CHOP-dependent ATF4 peaks within associated regulatory elements. ATF4 ESRGs containing CHOP-dependent ATF4 peaks are defined as CHOP-dependent ATF4 ESRGs, whereas those lacking such peaks are defined as CHOP-independent ATF4 ESRGs. (**C**) Heatmap showing expression patterns of CHOP-dependent and CHOP-independent ATF4 ESRGs in WT, ATF4-knockout, and CHOP-knockout cells under DMSO and Tm treatment conditions. (**D**) Box plots showing RNA expression levels of CHOP-dependent and CHOP-independent ATF4 ESRGs in WT, ATF4-knockout, and CHOP-knockout cells under DMSO and Tm treatment conditions. (**E**) Representative examples of CHOP-independent and CHOP-dependent ATF4 ESRGs. (**F**) RNA expression levels of *SLC43A1* and *TRIM25* in DMSO- and Tm-treated WT, ATF4-knockout, and CHOP-knockout cells. (**G**) GO enrichment analysis of CHOP-dependent and CHOP-independent ATF4 ESRGs.

CHOP-independent ATF4 ESRGs retained substantial induction in CHOP-knockout cells, while remaining dependent on ATF4. Thus, CHOP selectively influences the output of a subset of ATF4-regulated genes rather than globally controlling all ATF4-dependent transcription.

GO analysis revealed clear functional divergence between the two groups (Fig. 7G). CHOP-independent ATF4 ESRGs were enriched for amino acid transport-related processes, whereas CHOP-dependent ATF4 ESRGs were enriched for pathways associated with the ER stress response and ER stress-induced apoptosis. These findings suggest that CHOP selectively broadens the functional output of ATF4 by enabling activation of specific stress-responsive gene programs.

Together, these results show that CHOP does not simply enhance ATF4 activity globally, but instead diversifies ATF4-dependent transcriptional regulation during ER stress by selectively supporting a distinct subset of ATF4 target genes.

ATF4–CHOP cooperation balances adaptive and apoptotic transcriptional programs during ER stress

Building on our observation that CHOP selectively diversifies ATF4-dependent gene programs, we next asked how these regulatory differences influence adaptive and apoptotic responses during ER stress. To address this, we first examined two functionally distinct subsets of ATF4 ESRGs: amino acid transport-related genes and apoptosis-related genes. In WT cells, both groups were induced by Tm treatment, and this induction was markedly reduced in ATF4-knockout cells (Fig. 8A–D), confirming their dependence on ATF4. However, these two gene classes differed in their dependence on CHOP. Expression of amino acid transport-related ATF4 ESRGs was largely preserved in CHOP-knockout cells, whereas apoptosis-related ATF4 ESRGs were substantially reduced (Fig. 8A–D). These findings indicated that ATF4 independently regulates adaptive transcriptional programs, whereas induction of apoptotic gene programs requires cooperative ATF4–CHOP activity.

To define the underlying regulatory mechanisms at representative loci, we next examined *SLC7A5* and *TRIB3*, which typify CHOP-independent and CHOP-dependent ATF4 regulation, respectively. At the *SLC7A5* locus, Tm treatment increased ATF4 occupancy at a distal enhancer located ∼85 kb upstream of the promoter, accompanied by elevated H3K27ac levels and strengthened enhancer–promoter interactions (Fig. 8E). These changes were abolished in ATF4-knockout cells but were largely unaffected by CHOP depletion, consistent with the classification of this site as CHOP-optional. Accordingly, *SLC7A5* expression was strongly induced by Tm in WT cells, markedly reduced in ATF4-knockout cells, and largely preserved in CHOP-knockout cells (Fig. 8G).

In contrast, the *TRIB3* locus showed a distinct regulatory pattern. A CHOP-dependent ATF4 peak was detected at an enhancer located ∼15 kb downstream of the promoter, and Tm treatment increased the ATF4 occupancy, H3K27ac levels, and enhancer–promoter contact frequency at this site (Fig. 8F). Strikingly, both ATF4 and CHOP knockout abolished enhancer activation and chromatin looping at the *TRIB3* locus, indicating that cooperative ATF4–CHOP binding is required for regulatory activity at this site. Consistent with these chromatin changes, *TRIB3* expression was significantly reduced in both ATF4- and CHOP-knockout cells (Fig. 8H). Together, these locus-specific analyses indicate that ATF4 can activate distinct gene programs through mechanistically separable enhancer modules: a CHOP-independent mode exemplified by *SLC7A5* and a CHOP-dependent cooperative mode exemplified by *TRIB3*.

We next asked whether these transcriptional differences translate into functional cellular outcomes. Because amino acid transport genes represented a prominent CHOP-independent ATF4 program, we measured amino acid uptake capacity using BPA uptake assays. Tm treatment increased amino acid uptake in WT cells, and this response was markedly reduced in ATF4-knockout cells but remained largely intact in CHOP-knockout cells (Fig. 9A and C). We then assessed apoptosis under ER stress by Annexin V and propidium iodide staining. In contrast to amino acid uptake, ER stress-induced apoptosis was significantly attenuated in both ATF4- and CHOP-knockout cells relative to WT cells (Fig. 9B and D). These findings demonstrate that adaptive and apoptotic outputs of the ER stress response differ in their dependence on CHOP.

Taken together, these results show that ATF4 preferentially drives adaptive responses such as amino acid transport, whereas apoptotic outcomes depend more strongly on cooperative regulation by ATF4 and CHOP. At the chromatin level, this distinction is reflected in the differential use of enhancer modules and enhancer–promoter looping configurations. We therefore propose that ATF4–CHOP cooperation within a three-dimensional enhancer network functionally partitions adaptive and apoptotic transcriptional programs during ER stress, thereby shaping the balance between survival-promoting and pro-apoptotic responses (the "Graphical abstract" section).

Discussion

In this study, we provide a comprehensive multi-omics analysis of transcriptional regulation under ER stress. By integrating transcriptomic, epigenomic, chromatin interaction, and genetic perturbation data, we identify enhancer activation and chromatin looping as key regulatory features of ESRG expression.

ER stress induced a global increase in H3K27ac at distal regulatory elements and extensive reconfiguration of enhancer–promoter interactions, whereas chromatin accessibility and higher-order chromatin structures such as A/B compartments and TAD boundaries remained largely stable. These findings suggest that ER stress-responsive transcription is achieved through selective modulation of regulatory element activity and connectivity within an otherwise stable chromatin framework. Thus, rather than being driven by large-scale chromatin reorganization, transcriptional reprogramming under ER stress appears to depend primarily on changes in enhancer activity and enhancer–promoter communication.

A key finding of this study is the identification of ATF4 as a dominant regulator of enhancer activation and chromatin looping during ER stress. Across multiple independent analyses, including correlation of TF binding with H3K27ac induction, loss-of-function perturbation, and chromatin interaction profiling, ATF4 consistently showed the strongest effect on both enhancer activity and loop formation. Notably, ATF4 depletion caused the most pronounced reduction in stress-induced H3K27ac accumulation and markedly

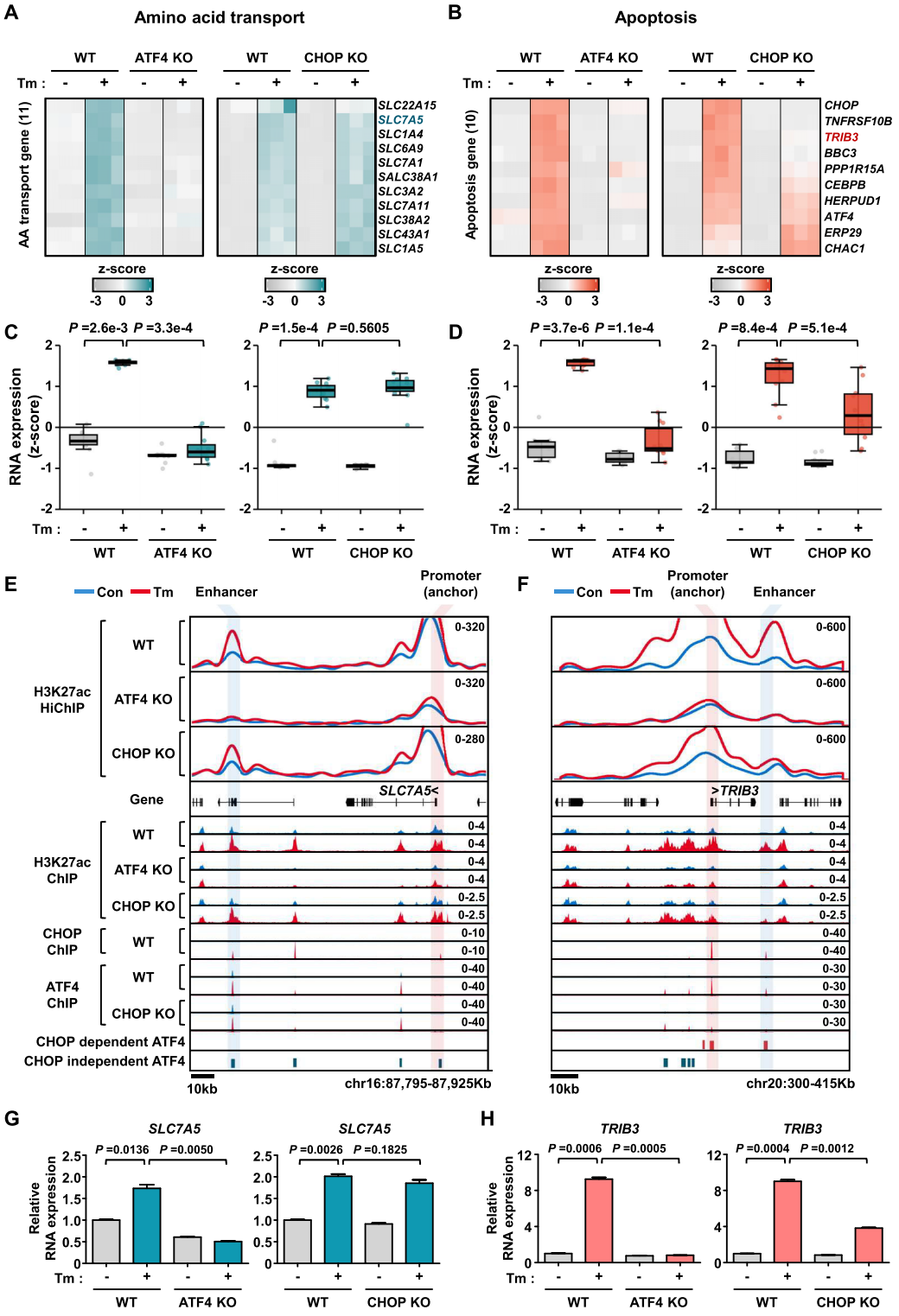

Figure 8. ATF4–CHOP cooperation balances adaptive and apoptotic transcriptional programs during ER stress. (**A**) Heatmap showing expression patterns of amino acid transport-related ATF4 ESRGs in WT, ATF4-knockout, and CHOP-knockout cells under DMSO and Tm treatment conditions. (**B**) Heatmap showing expression patterns of apoptosis-related ATF4 ESRGs in WT, ATF4-knockout, and CHOP-knockout cells under DMSO and Tm treatment conditions. (**C**) Box plots showing RNA expression levels of amino acid transport-related ATF4 ESRGs in WT, ATF4-knockout, and CHOP-knockout cells under DMSO and Tm treatment conditions. (**D**) Box plots showing RNA expression levels of apoptosis-related ATF4 ESRGs in WT, ATF4-knockout, and CHOP-knockout cells under DMSO and Tm treatment conditions. (**E**) Genome browser view of the *SLC7A5* locus showing enhancer activation and chromatin loop dynamics consistent with a CHOP-independent mode of ATF4-mediated transcriptional regulation. Tracks shown include ATF4 ChIP-seq signal, H3K27ac ChIP-seq signal, H3K27ac HiChIP interactions, and RNA expression in the indicated genotypes and treatment conditions. (**F**) Genome browser view of the *TRIB3* locus showing enhancer activation and chromatin loop dynamics consistent with a CHOP-dependent cooperative mode of ATF4-mediated transcriptional regulation. Tracks shown include ATF4 ChIP-seq signal, H3K27ac ChIP-seq signal, H3K27ac HiChIP interactions, and RNA expression in the indicated genotypes and treatment conditions. (**G**) RNA expression levels of *SLC7A5* in DMSO- and Tm-treated WT, ATF4-knockout, and CHOP-knockout cells. (**H**) RNA expression levels of *TRIB3* in DMSO- and Tm-treated WT, ATF4-knockout, and CHOP-knockout cells.

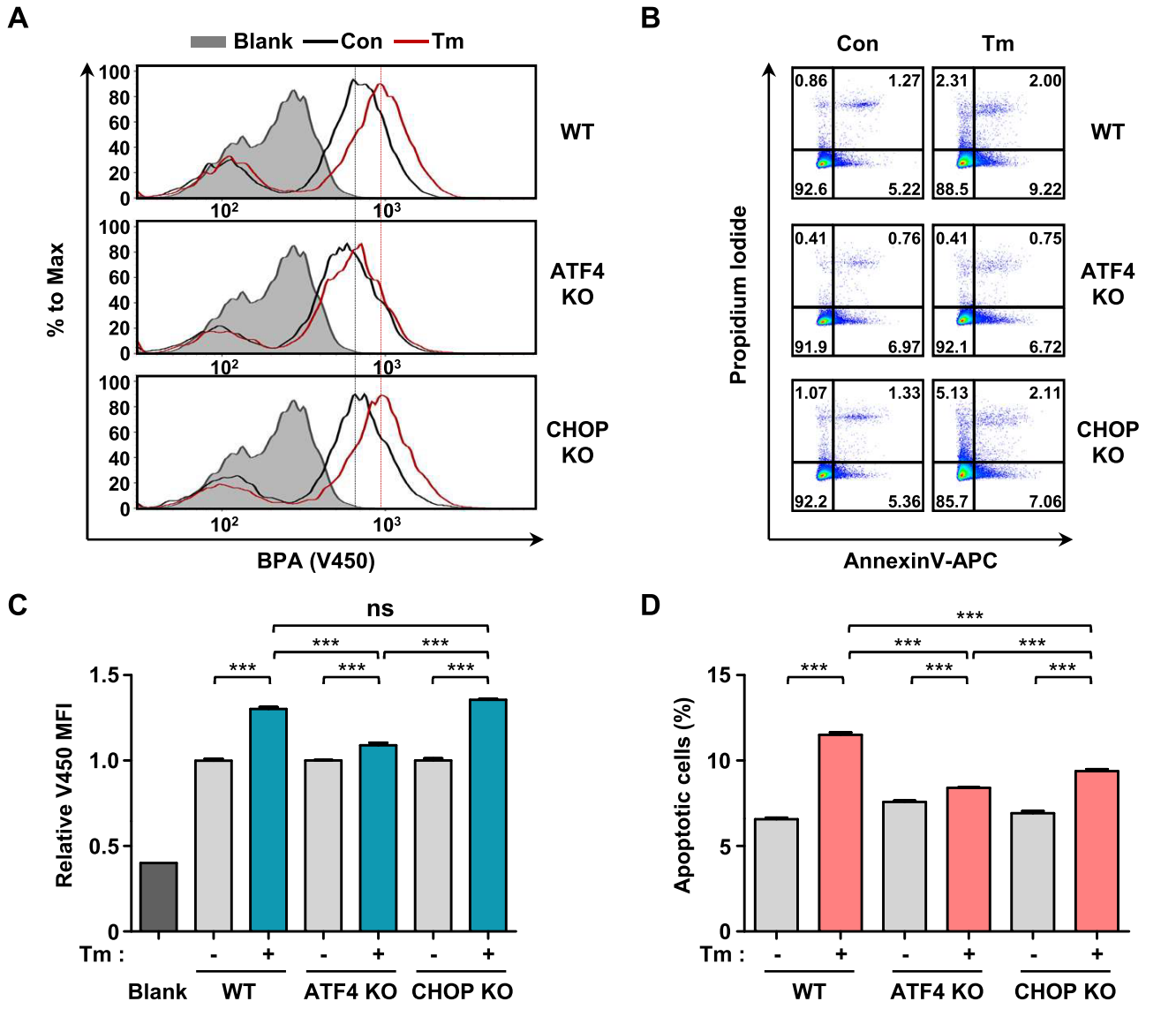

Figure 9. ATF4–CHOP cooperation determines functional outcomes of ER stress responses. (**A**) Amino acid uptake capacity measured by flow cytometry in WT, ATF4-knockout, and CHOP-knockout cells using BPA uptake. The fluorescence intensity reflects the amino acid uptake capacity. (**B**) ER stress-induced apoptosis assessed by Annexin V and propidium iodide staining in WT, ATF4-knockout, and CHOP-knockout cells. (**C**) Bar plots showing mean fluorescence intensity (MFI) of V450-BPA as a measure of the amino acid uptake capacity. MFIs in Tm-treated cells were normalized to those in DMSO-treated cells for each genotype. (**D**) Percentages of apoptotic cells under ER stress conditions in WT, ATF4-knockout, and CHOP-knockout cells.

attenuated chromatin looping, including at SEs. These observations establish ATF4 as a central organizer of the enhancer-centered chromatin interaction network underlying ER stress-responsive transcription.

Our results further demonstrate that ATF4-dependent enhancers are functionally coupled to long-range chromatin interactions that regulate gene expression. At representative loci such as *BBS10*, ATF4 binding at distal enhancers was associated with increased H3K27ac, strengthened enhancer–promoter contacts, and transcriptional activation, all of which were abolished by ATF4 depletion. Live-cell imaging using a Casilio-based system independently confirmed stress-induced spatial proximity between enhancers and promoters in an ATF4-dependent manner. Together, these findings support a model in which ATF4 couples enhancer activation to long-range chromatin interactions, thereby enabling transcriptional regulation over long genomic distances.

While ATF4 exerts broad control over enhancer activation, our data indicate that transcriptional specificity is achieved through combinatorial interactions with other TFs. In particular, we identify CHOP as a key modulator of ATF4 function. CHOP selectively influences ATF4 genomic occupancy at a subset of regulatory elements without substantially altering ATF4 protein abundance, indicating that its effect is exerted at the level of chromatin occupancy rather than TF abundance. Consistent with this, CHOP depletion resulted in selective loss of ATF4 binding and H3K27ac specifically at CHOP-dependent ATF4 sites, while leaving other ATF4-bound regions largely unaffected. These findings extend previous promoter-centered models of ATF4–CHOP cooperation by showing that partner-dependent diversification also operates at the level of enhancer activation and chromatin looping.

Previous studies have established that ATF4 and CHOP cooperate in multiple stress-responsive transcriptional

programs, including autophagy, apoptosis, and amino acid-responsive gene regulation [50–52]. For example, the eIF2α–ATF4 pathway has been shown to direct stress-induced autophagy gene expression, with different combinations of ATF4 and CHOP binding contributing to distinct transcriptional outputs across autophagy-related genes. Likewise, ER stress-induced activation of the TRIB3 promoter has been linked to cooperative ATF4–CHOP regulation and to apoptosis-associated signaling. In addition, CHOP has been shown to modulate ATF4-dependent transcription in a gene-specific manner during amino acid response, enhancing induction of some targets such as TRIB3 while repressing others such as ASNS. Our findings are broadly consistent with these earlier studies, but extend them in an important way. Whereas prior work largely defined ATF4–CHOP function in promoter-centered terms and at the level of individual target genes, our data indicate that this cooperation also operates at the level of enhancer activation and chromatin looping. In this framework, ATF4 establishes a broad enhancer-associated regulatory architecture, whereas CHOP selectively modulates a subset of ATF4-bound regulatory elements to diversify transcriptional outputs, including the differential control of adaptive and apoptotic gene programs.

This selective modulation is reflected at the level of gene regulation. By stratifying ATF4 target genes based on CHOP dependency, we show that ATF4 can regulate a subset of genes associated with adaptive responses (e.g. amino acid transport), largely independently of CHOP, whereas activation of genes linked to ER stress response and apoptosis depends more strongly on cooperative ATF4–CHOP activity. Locus-specific analyses further support this model: at the *SLC7A5* locus, enhancer activation and chromatin looping are ATF4-dependent but CHOP-independent; whereas at the *TRIB3* locus, both processes require the combined action of ATF4 and CHOP. Functionally, this regulatory architecture enables differential control of adaptive and apoptotic responses under ER stress. Consistent with gene expression patterns, amino acid uptake was dependent on ATF4 but largely unaffected by CHOP depletion, whereas ER stress-induced apoptosis required both ATF4 and CHOP.

Taken together, our data argue against a simple binary model in which ATF4 is exclusively adaptive and CHOP is exclusively pro-apoptotic. Instead, ER stress-responsive transcription appears to be organized hierarchically: ATF4 establishes a broad regulatory scaffold by promoting enhancer activation and chromatin looping across the stress-responsive genome, whereas interacting partners such as CHOP selectively refine this architecture at specific loci. In this framework, ATF4 supports a broad stress-responsive regulatory program, while CHOP biases its transcriptional output toward specific programs, including apoptosis-associated gene expression. This interpretation is consistent with the emerging view that UPR signaling functions as a context-dependent rheostatic network in which adaptive and terminal responses are tuned according to the stress severity and duration.

Recent work on the integrated stress response has suggested that selective ATF4-dependent transcription can arise from pre-established chromatin states and promoter-proximal occupancy, with limited dependence on widespread chromatin remodeling [23]. Our findings do not exclude such mechanisms at a subset of loci. However, in the ER stress context examined here, enhancer activation and chromatin looping make prominent contributions to transcriptional regulation, particularly at distal regulatory elements and CHOP-dependent loci. These observations suggest that ATF4-dependent stress responses may be implemented through distinct regulatory modes depending on stress context, locus class, and TF partnership.

Several limitations of this study should be noted. Our analyses were performed in a defined ER stress model and were designed to define the regulatory architecture of ATF4- and CHOP-dependent transcription specifically in the context of ER stress. Accordingly, the extent to which the enhancer activation and chromatin-looping mechanisms identified here are conserved across other integrated stress response inputs, such as amino acid starvation, remains to be determined. In addition, although multi-omics integration, loss-of-function analyses, and locus-specific assays strongly support the involvement of ATF4 and CHOP in enhancer activation and chromatin looping, not all candidate regulatory interactions were directly tested for causality. As a result, the present study may underrepresent context-specific regulatory variation and may not fully resolve the relative contribution of individual enhancers or chromatin contacts at every target locus. Addressing these questions will require future studies in distinct stress contexts, multiple cellular models, diverse ER stress conditions and time courses, and systematic perturbation of candidate enhancers and loop anchors. Such work will help clarify which features of ATF4–CHOP-dependent regulation are shared versus context-specific and further define the causal logic of this regulatory framework.

Our study highlights the importance of integrating enhancer activity with long-range chromatin interactions to understand stimulus-responsive transcriptional regulation. Despite the limitations noted above, the principles described here—a broad regulatory network established by a primary TF and selectively refined by interacting partners—may represent a general mechanism by which cells achieve both robustness and specificity in gene regulation under stress conditions.

Acknowledgements

Author contributions: Jung-Sik Joo (Data curation [equal], Formal analysis [equal], Resources [lead], Validation [lead], Writing—original draft [lead]), Mikyoung Kim (Formal analysis [supporting], Visualization [supporting]), Sugyung Kim (Formal analysis [supporting]), Hyejin Kim (Formal analysis [supporting]), and Hyoung-Pyo Kim (Conceptualization [equal], Data curation [equal], Formal analysis [equal], Funding acquisition [equal], Investigation [equal], Project administration [equal], Supervision [lead], Writing—review & editing [lead]).

Supplementary data

Supplementary data is available at NAR online.

Conflict of interest

None declared.

Funding

This study was supported by The National Research Foundation of Korea (NRF), funded by the Korean government (MSIP) (RS-2025-00562938 and RS-2025-02304471 to

H.-P.K.) and by a Yonsei-SCL research grant of Yonsei University College of Medicine (6-2025-0106 to H.-P.K.).

Data availability

All RNA-seq, ChIP-seq, ATAC-seq, *in situ* Hi-C, and HiChIP data generated in this study were deposited in the GEO (https://www.ncbi.nlm.nih.gov/geo/) under the accession numbers: GSE324345 (RNA-Seq), GSE324343 (ChIP-Seq), GSE324342 (ATAC-Seq), GSE324344 (*in situ* Hi-C), and GSE324346 (HiChIP). UCSC Genome Browser sessions for RNA-seq, ChIP-seq, ATAC-seq, *in situ* Hi-C, and HiChIP data generated in this study are available at the following URLs: https://genome.ucsc.edu/s/EMB_Lab/UPR_genome%2Dwide%20binding%20data%20SET; https://genome.ucsc.edu/s/EMB_Lab/UPR_expression%20data%20SET; and https://genome.ucsc.edu/s/EMB_Lab/UPR_interaction%20data%20SET.

References

1. Hetz C. The unfolded protein response: controlling cell fate decisions under ER stress and beyond. *Nat Rev Mol Cell Biol* 2012;13:89–102. https://doi.org/10.1038/nrm3270
2. Hetz C, Papa FR. The unfolded protein response and cell fate control. *Mol Cell* 2018;69:169–81. https://doi.org/10.1016/j.molcel.2017.06.017
3. Acosta-Alvear D, Harnoss JM, Walter P *et al.* Homeostasis control in health and disease by the unfolded protein response. *Nat Rev Mol Cell Biol* 2025;26:193–212. https://doi.org/10.1038/s41580-024-00794-0
4. Nwosu GO, Powell JA, Pitson SM. Targeting the integrated stress response in hematologic malignancies. *Exp Hematol Oncol* 2022;11:94. https://doi.org/10.1186/s40164-022-00348-0
5. Wortel IMN, van der Meer LT, Kilberg MS *et al.* Surviving stress: modulation of ATF4-mediated stress responses in normal and malignant cells. *Trends Endocrinol Metab* 2017;28:794–806. https://doi.org/10.1016/j.tem.2017.07.003
6. Hetz C, Zhang K, Kaufman RJ. Mechanisms, regulation and functions of the unfolded protein response. *Nat Rev Mol Cell Biol* 2020;21:421–38. https://doi.org/10.1038/s41580-020-0250-z
7. Carreras-Sureda A, Kroemer G, Cardenas JC *et al.* Balancing energy and protein homeostasis at ER-mitochondria contact sites. *Sci Signal* 2022;15:eabm7524. https://doi.org/10.1126/scisignal.abm7524
8. Shoulders MD, Ryno LM, Genereux JC *et al.* Stress-independent activation of XBP1s and/or ATF6 reveals three functionally diverse ER proteostasis environments. *Cell Rep* 2013;3:1279–92. https://doi.org/10.1016/j.celrep.2013.03.024
9. Nair R, A. L, P. Z *et al.* A permissive epigenetic landscape facilitates distinct transcriptional signatures of activating transcription factor 6 in the liver. *Genomics* 2022;114:107–24. https://doi.org/10.1016/j.ygeno.2021.11.034
10. Pramanik J, Chen X, Kar G *et al.* Genome-wide analyses reveal the IRE1a–XBP1 pathway promotes T helper cell differentiation by resolving secretory stress and accelerating proliferation. *Genome Med* 2018;10:76. https://doi.org/10.1186/s13073-018-0589-3
11. Ferguson DC, McCorkle JR, Barnett KR *et al.* Amino acid stress response genes promote L-asparaginase resistance in pediatric acute lymphoblastic leukemia. *Blood Adv* 2022;6:3386–97. https://doi.org/10.1182/bloodadvances.2022006965
12. Smale ST. Selective transcription in response to an inflammatory stimulus. *Cell* 2010;140:833–44. https://doi.org/10.1016/j.cell.2010.01.037
13. Xie S, Armendariz D, Zhou P *et al.* Global analysis of enhancer targets reveals convergent enhancer-driven regulatory modules. *Cell Rep* 2019;29:2570–8. https://doi.org/10.1016/j.celrep.2019.10.073
14. Stanek TJ, Gennaro VJ, Tracewell MA *et al.* The SAGA complex regulates early steps in transcription via its deubiquitylase module subunit USP22. *EMBO J* 2021;40:e102509. https://doi.org/10.15252/embj.2019102509
15. Daniel PV, Erickson HL, Choi D *et al.* ER stress upregulates S100A11 in steatohepatitis models via epigenetic modifications within the lipotoxicity-influenced enhancer. *J Clin Invest* 2025;135:e191074. https://doi.org/10.1172/JCI191074
16. Wang A, Yan S, Liu J *et al.* Endoplasmic reticulum stress-related super enhancer promotes epithelial-mesenchymal transformation in hepatocellular carcinoma through CREB5 mediated activation of TNC. *Cell Death Dis* 2025;16:73. https://doi.org/10.1038/s41419-025-07356-y
17. Dubois V, Gheeraert C, Vankrunkelsven W *et al.* Endoplasmic reticulum stress actively suppresses hepatic molecular identity in damaged liver. *Mol Syst Biol* 2020;16:e9156. https://doi.org/10.15252/msb.20199156
18. Li M, Yao T, Lin W *et al.* Double DAP-seq uncovered synergistic DNA binding of interacting bZIP transcription factors. *Nat Commun* 2023;14:2600. https://doi.org/10.1038/s41467-023-38096-2
19. Vinson CR, Hai T, Boyd SM. Dimerization specificity of the leucine zipper-containing bZIP motif on DNA binding: prediction and rational design. *Genes Dev* 1993;7:1047–58. https://doi.org/10.1101/gad.7.6.1047
20. Pogenberg V, Consani Textor L, Vanhille L *et al.* Design of a bZip transcription factor with homo/heterodimer-induced DNA-binding preference. *Structure* 2014;22:466–77. https://doi.org/10.1016/j.str.2013.12.017
21. Rodriguez-Martinez JA, Reinke AW, Bhimsaria D *et al.* Combinatorial bZIP dimers display complex DNA-binding specificity landscapes. *eLife* 2017;6:e19272. https://doi.org/10.7554/eLife.19272
22. Kim D, Kim J, Yu YS *et al.* Systemic approaches using single cell transcriptome reveal that C/EBPgamma regulates autophagy under amino acid starved condition. *Nucleic Acids Res* 2022;50:7298–309. https://doi.org/10.1093/nar/gkac593
23. Jiang P, Bian Q. Pre-established ATF4 occupancy and chromatin organization instruct selective transcription activation during integrated stress response. *Nat Commun* 2025;16:9502. https://doi.org/10.1038/s41467-025-64577-7
24. Wang Q, Mora-Jensen H, Weniger MA *et al.* ERAD inhibitors integrate ER stress with an epigenetic mechanism to activate BH3-only protein NOXA in cancer cells. *Proc Natl Acad Sci USA* 2009;106:2200–5. https://doi.org/10.1073/pnas.0807611106
25. Han J, Back SH, Hur J *et al.* ER-stress-induced transcriptional regulation increases protein synthesis leading to cell death. *Nat Cell Biol* 2013;15:481–90. https://doi.org/10.1038/ncb2738
26. Huggins CJ, Mayekar MK, Martin N *et al.* C/EBPgamma is a critical regulator of cellular stress response networks through heterodimerization with ATF4. *Mol Cell Biol* 2015;36:693–713. https://doi.org/10.1128/MCB.00911-15
27. Cohen DM, Won KJ, Nguyen N *et al.* ATF4 licenses C/EBPbeta activity in human mesenchymal stem cells primed for adipogenesis. *eLife* 2015;4:e06821. https://doi.org/10.7554/eLife.06821
28. Lee EC, Kim K, Kim S *et al.* 3D enhancer architecture coordinated by CTCF determines immune-related gene expression patterns via RNA polymerase II pause-release in CD4+ T cells. *Nucleic Acids Res* 2025;53:gkaf1404. https://doi.org/10.1093/nar/gkaf1404
29. Dobin A, Davis CA, Schlesinger F *et al.* STAR: ultrafast universal RNA-seq aligner. *Bioinformatics* 2013;29:15–21. https://doi.org/10.1093/bioinformatics/bts635
30. Li B, Dewey CN. RSEM: accurate transcript quantification from RNA-Seq data with or without a reference genome. *BMC Bioinf* 2011;12:323. https://doi.org/10.1186/1471-2105-12-323
31. Li H, Handsaker B, Wysoker A *et al.* Genome Project Data Processing, S *et al.*. The Sequence Alignment/Map format and

SAMtools. *Bioinformatics* 2009;25:2078–9. https://doi.org/10.1093/bioinformatics/btp352
32. Ramirez F, Dundar F, Diehl S *et al.* deepTools: a flexible platform for exploring deep-sequencing data. *Nucleic Acids Res* 2014;42:W187–191. https://doi.org/10.1093/nar/gku365
33. Love MI, Huber W, Anders S. Moderated estimation of fold change and dispersion for RNA-seq data with DESeq2. *Genome Biol* 2014;15:550. https://doi.org/10.1186/s13059-014-0550-8
34. Yu G, Wang LG, Han Y *et al.* clusterProfiler: an R package for comparing biological themes among gene clusters. *OMICS* 2012;16:284–7. https://doi.org/10.1089/omi.2011.0118
35. Langmead B, Salzberg SL. Fast gapped-read alignment with Bowtie 2. *Nat Methods* 2012;9:357–9. https://doi.org/10.1038/nmeth.1923
36. Zhang Y, Liu T, Meyer CA *et al.* Model-based analysis of ChIP-Seq (MACS). *Genome Biol* 2008;9:R137. https://doi.org/10.1186/gb-2008-9-9-r137
37. Li H, Durbin R. Fast and accurate short read alignment with Burrows–Wheeler transform. *Bioinformatics* 2009;25:1754–60. https://doi.org/10.1093/bioinformatics/btp324
38. Whyte WA, Orlando DA, Hnisz D *et al.* Master transcription factors and mediator establish super-enhancers at key cell identity genes. *Cell* 2013;153:307–19. https://doi.org/10.1016/j.cell.2013.03.035
39. Servant N, Varoquaux N, Lajoie BR *et al.* HiC-Pro: an optimized and flexible pipeline for Hi-C data processing. *Genome Biol* 2015;16:259. https://doi.org/10.1186/s13059-015-0831-x
40. Chakraborty A, Wang JG, Ay F. dcHiC detects differential compartments across multiple Hi-C datasets. *Nat Commun* 2022;13:6827. https://doi.org/10.1038/s41467-022-34626-6
41. Open2 C, Abdennur N, Abraham S *et al.* Cooltools: enabling high-resolution Hi-C analysis in Python. *PLoS Comput Biol* 2024;20:e1012067.
42. Bhattacharyya S, Chandra V, Vijayanand P *et al.* Identification of significant chromatin contacts from HiChIP data by FitHiChIP. *Nat Commun* 2019;10:4221. https://doi.org/10.1038/s41467-019-11950-y
43. Quinlan AR, Hall IM. BEDTools: a flexible suite of utilities for comparing genomic features. *Bioinformatics* 2010;26:841–2. https://doi.org/10.1093/bioinformatics/btq033
44. Wozniak T, Sura W, Kazimierska M *et al.* TransCRISPR-sgRNA design tool for CRISPR/Cas9 experiments targeting specific sequence motifs. *Nucleic Acids Res* 2023;51:W577–86. https://doi.org/10.1093/nar/gkad355
45. Montague TG, Cruz JM, Gagnon JA *et al.* CHOPCHOP: a CRISPR/Cas9 and TALEN web tool for genome editing. *Nucleic Acids Res* 2014;42:W401–407. https://doi.org/10.1093/nar/gku410
46. Williams J, Hurling C, Munir S *et al.* Modelling renal defects in Bardet–Biedl syndrome patients using human iPS cells. *Front Cell Dev Biol* 2023;11:1163825. https://doi.org/10.3389/fcell.2023.1163825
47. Stoetzel C, Laurier V, Davis EE *et al.* BBS10 encodes a vertebrate-specific chaperonin-like protein and is a major BBS locus. *Nat Genet* 2006;38:521–4. https://doi.org/10.1038/ng1771
48. Clow PA, Du M, Jillette N *et al.* CRISPR-mediated multiplexed live cell imaging of nonrepetitive genomic loci with one guide RNA per locus. *Nat Commun* 2022;13:1871. https://doi.org/10.1038/s41467-022-29343-z
49. Bailey TL, Boden M, Buske FA *et al.* MEME SUITE: tools for motif discovery and searching. *Nucleic Acids Res* 2009;37:W202–208. https://doi.org/10.1093/nar/gkp335
50. Su N, Kilberg MS. C/EBP homology protein (CHOP) interacts with activating transcription factor 4 (ATF4) and negatively regulates the stress-dependent induction of the asparagine synthetase gene. *J Biol Chem* 2008;283:35106–17. https://doi.org/10.1074/jbc.M806874200
51. B'chir W, Maurin A-C, Carraro V *et al.* The eIF2α/ATF4 pathway is essential for stress-induced autophagy gene expression. *Nucleic Acids Res* 2013;41:7683–99.
52. Ohoka N, Yoshii S, Hattori T *et al.* TRB3, a novel ER stress-inducible gene, is induced via ATF4–CHOP pathway and is involved in cell death. *EMBO J* 2005;24:1243–55. https://doi.org/10.1038/sj.emboj.7600596

Received: April 9, 2026. **Revised:** June 2, 2026. **Accepted:** June 5, 2026